

Numerical investigations of the effects of spanwise grooves on the suppression of vortex-induced vibration of a flexible cylinder

Bo Han^a, Luchun Yang^b, Weiwen Zhao^a, Decheng Wan^{a,*}

^a Computational Marine Hydrodynamics Lab (CMHL), School of Naval Architecture, Ocean and Civil Engineering, Shanghai Jiao Tong University, Shanghai, 200240, China

^b Wuhan Second Ship Design and Research Institute, Wuhan, 430205, China

ARTICLE INFO

Keywords:

VIV suppression
Uniform flow
viv3D-FOAM-SJTU solver
Spanwise grooves

ABSTRACT

Numerical investigations of Vortex-induced Vibration (VIV) suppression of a flexible cylinder with spanwise grooves in the uniform flow have been conducted by viv3D-FOAM-SJTU solver, which imports the thick strip model into OpenFOAM. The Reynolds-averaged Navier-Stokes (RANS) method is adopted to calculate hydrodynamic forces at each fluid strip. The vibrations of cylinder are solved through the Euler-Bernoulli bending beam hypothesis and the Finite Element Method (FEM) in two directions. During simulations, four spanwise grooves are arranged equally around the cylinder with an interval of 90° at two configurations. The spanwise groove keeps a constant width of $w = 0.2D$ and a variable groove depth among $0.08D$, $0.12D$ and $0.16D$. Specific comparisons on Root Mean Square (RMS) vibration displacements, vibration modal responses, vibration frequency responses and vortex structures are conducted to analyze suppression effects of the spanwise grooves. Numerical studies indicate that the appropriate choose of groove geometry and arrangement can effectively reduce both crossflow and inline VIV responses.

1. Introduction

Vortex-induced Vibration (VIV) of marine risers is of practical interest to offshore oil and gas production. As a typical fluid-structure interaction phenomenon, VIV involves complex responses of multi-mode vibrations, mode transitions, etc. Some comprehensive reviews written by Bearman (1984) [1], Sumer and Fredsøe (1997) [2], Sarpkaya (2004) [3], Gabbai and Benaroya (2005) [4], Williamson and Govardhan (2004, 2008) [5,6], Huang et al. (2009) [7], Wu et al. (2012) [8], Chen et al. (2016) [9] and Wan and Duanmu (2017) [10] can be referred. VIV has been proven to be a major source that contribute to fatigue damage of marine risers. Therefore, various control methods have been studied by researchers and applied in practical productions to suppress VIV responses of risers in the past decades.

At present, VIV suppression methods are mainly divided into two classes: the active control and the passive control. The active control strategies require additional energy input outside risers to realize VIV suppression during the production. Some investigations on active control methods can be found in Wu et al. (2007) [11], Korkischko and Meneghini (2012) [12], Chen et al. (2013) [13] and Feng et al. (2010) [14]. The passive control methods have been widely used in ocean engineering due to their low economical costs and convenient applications comparing to the active control methods. Common passive VIV suppression devices mainly include: helical strakes, control rods, demarcation strips, fairings, spoilers and etc.

* Corresponding author.

E-mail address: dcwan@sjtu.edu.cn (D. Wan).

The helical strakes are the most widely used in offshore engineering and academic research compared to other passive devices. Zhou et al. (2011) [15] conducted experiments of a circular cylinder with three-start helical strakes in a wind tunnel. Vortex shedding and dominant frequency features were analyzed in detail. Ranjith et al. (2016) [16] carried out three-dimensional numerical simulations of a circular cylinder with three-start helical strakes. They found that the helical strakes could reduce VIV responses by 99%. Gao et al. (2016) [17] studied the effects of different helical strake coverages on VIV responses of a flexible cylinder in the uniform and linearly sheared flows respectively. They found that the flexible cylinder presented the best comprehensive evaluation with 75% helical strake coverage in the uniform flow, while it decreased to 50% helical strake coverage in the linearly sheared flow. Similar model experiments have also been conducted by Trim et al. (2005) [18] and Vandiver et al. (2006) [19]. Vandiver et al. (2006) [19] and Bourguet et al. (2011) [20] discussed that the trajectory of the cylinder is significant on whether energy is being transferred to or from the fluid at particular locations along the length of the flexible cylinder. Quen et al. (2014) [21] carried out experiments of a flexible cylinder with different helical strakes in the uniform flow. They found that the most effective configuration of strakes is $p = 10D$ and $h = 0.15D$ (where p is the pitch, h is the height and D is the cylinder diameter) in terms of dynamic responses reduction. Furtherly, Quen et al. (2018) [22] studied the VIV suppression effects of a flexible cylinder with two- and three-start helical strakes respectively. Xu et al. (2017) [23] investigated VIV suppression of an inclined flexible cylinder fitted with helical strakes experiencing the uniform flow in a towing tank. They concluded that VIV suppression effectiveness was closely related to the yaw angle of the cylinder to the incoming flow. Ren et al. (2019) [24] also studied VIV suppression effects of helical strakes to a flexible cylinder experiencing the oscillatory flow. Although, the helical strakes can greatly reduce crossflow VIV responses, it will apparently increase the drag coefficient that leads to the enlargement of inline VIV responses, such as the mean inline deflection and inline RMS displacements.

As for other passive control devices, Song et al. (2017) [25] numerically studied flow past a circular cylinder with three control rods. Effects of the attack angle and the rod-to-cylinder gap on VIV suppression effectiveness were mainly investigated. Zhu et al. (2015) [26] and Lu et al. (2019) [27] also conducted similar numerical researches. Li et al. (2020) [28] carried out experiments of a riser fitted with discrete spoiler in the uniform flow. Nikoo et al. (2018) [29] carried out three-dimensional numerical simulations of a pip-in-pip (PIP) system to study its VIV suppression effectiveness. Hu et al. (2021) [30] analyzed the contribution of VIV suppression of double tail splitter plates with experiment. Although, these methods can effectively reduce VIV responses of risers in different ways, the complexity of its installation contributes to the limitations of its practical application in actual production.

Instead of installing extra passive devices to change the surface and buoyancy feature of the riser, the surface modification method can offer an optional way in both reducing vibration displacements and hydrodynamic forces. Huang (2011) [31] carried out experiments to investigate effects of three-start helical grooves on the drag reduction of a fixed circular cylinder and VIV responses of an elastically supported cylinder. They found that the helical grooves could effectively reduce both crossflow VIV amplitude and inline drag coefficient. While different diameters are used in the normalization of the drag force, and the grooves in the experiment are not small enough to be ignored, which means in order to guarantee a proper thickness of the riser wall, larger diameters are necessary for the cylinders with grooves. Law and Jaiman (2018) [32] numerically studied VIV suppression effects of a surface-modification based device, the spanwise grooves, on both deflection responses and the hydro-force responses of a circular cylinder. Two configurations of grooves, namely the staggered groove and the helical groove, were investigated. They found that the crossflow vibration amplitude and the drag force were suppressed up to 37% and 25% by the spanwise staggered grooves, which presented the best VIV suppression effectiveness. Zhou et al. (2015) [33] carried out experiments to investigate drag coefficient and flow characteristics of a longitudinally grooved cylinder. They found that the wake of a grooved cylinder was both more compact in the inline direction and narrower in the crossflow direction compared with that of the smooth cylinder at the same flow condition. Meanwhile, the reduction of the mean drag coefficient could reach up to 18%–28%. On the other hand, inappropriate arrangement of grooves could apparently magnify the VIV response of the cylinder [34–36].

However, most of these studies are concentrated on VIV suppression effects of spanwise grooves on circular cylinders and rare researches have been conducted to study the VIV suppression effectiveness of a grooved flexible cylinder. Therefore, numerical simulations of a long flexible cylinder with four-start longitudinal spanwise grooves experiencing the uniform flow are carried out using the CFD solver viv3D-FOAM-SJTU in present studies, which has been proved available in the VIV responses prediction of a flexible cylinder by Deng et al. (2020) [37]. The solver adopts the thick strip model in the numerical simulation, which provides 3-dimensional vortex shedding display at a series of positions, especially the vortex structure variation along the initial generatrix direction of the cylinder. Hu et al. (2022 and 2023) [38,39] have already conducted the numerical simulation and investigated the VIV suppression with symmetric double grooves and spanwise strips with the viv3D-FOAM-SJTU solver.

In present work, two configurations of four spanwise grooves with a constant width (w) and three different depths (d) are mainly examined. This paper is organized as followed: The first section briefly introduces the numerical method used in the present researches. The second section presents simulation setup and corresponding conditions. The third section gives detailed comparisons and analysis. Finally, the last section concludes the paper.

2. Numerical method

2.1. Hydrodynamic governing equations

Lift and drag forces acted on the cylinder surface are obtained through the integration of viscous force and pressure, calculated using the PIMPLE algorithm in each boundary mesh at each 3D fluid strip. For the incompressible viscous fluid, the continuity and the momentum equations can be written as follows:

$$\frac{\partial u_i}{\partial x_i} = 0 \quad (1)$$

$$\frac{\partial u_i}{\partial t} + \frac{\partial u_i u_j}{\partial x_j} = -\frac{1}{\rho} \frac{\partial p}{\partial x_i} + \frac{\partial}{\partial x_j} \left[\nu \left(\frac{\partial u_i}{\partial x_j} + \frac{\partial u_j}{\partial x_i} \right) \right] \quad (2)$$

where ρ is the constant fluid density, ν is the kinematic viscosity of the fluid.

The Reynolds-averaged Navier-Stokes (RANS) method is employed to solve the incompressible fluid flow, which has been proved to be available in VIV responses prediction of long flexible cylinder by many researchers, such as Duanmu et al. (2017, 2018) [40,41], Fu et al. (2018) [42] and Deng et al. (2020) [37]. After the time equal treatment, the RANS governing equations can be written as follows:

$$\frac{\partial \bar{u}_i}{\partial x_i} = 0 \quad (3)$$

$$\frac{\partial \bar{u}_i}{\partial t} + \frac{\partial \bar{u}_i \bar{u}_j}{\partial x_j} = -\frac{1}{\rho} \frac{\partial \bar{p}}{\partial x_i} + \frac{\partial}{\partial x_j} \left[\nu \left(\frac{\partial \bar{u}_i}{\partial x_j} + \frac{\partial \bar{u}_j}{\partial x_i} \right) \right] - \frac{1}{\rho} \frac{\partial \tau_{ij}^{RANS}}{\partial x_j} \quad (4)$$

where $\tau_{ij}^{RANS} = \overline{\rho u_i u_j}$ is the Reynolds stress.

The shear stress transport (SST) k - ω model is a hybrid k - ω and k - ϵ model proposed by Menter (1993) [43]. The model is employed for turbulence modeling to close the RANS equations. Transport equations of turbulence kinetic energy k and turbulence dissipation rate ω are given as Eq [34] and Eq [44].

$$\frac{\partial k}{\partial t} + \frac{\partial (u_j k)}{\partial x_j} = \tilde{G} - \beta^* \omega k + \frac{\partial}{\partial x_j} \left[(\nu + \alpha_k \nu_t) \frac{\partial k}{\partial x_j} \right] \quad (5)$$

$$\frac{\partial \omega}{\partial t} + \frac{\partial (u_j \omega)}{\partial x_j} = \gamma S^2 - \beta \omega^2 + \frac{\partial}{\partial x_j} \left[(\nu + \alpha_\omega \nu_t) \frac{\partial \omega}{\partial x_j} \right] + (1 - F_1) CD_{k\omega} \quad (6)$$

where $\tilde{G} = \min(\nu_t S^2, c_1 \beta^* k \omega)$, in which $S = \sqrt{2S_{ij}S_{ij}}$ and $S_{ij} = \frac{1}{2} \left(\frac{\partial u_i}{\partial x_j} + \frac{\partial u_j}{\partial x_i} \right)$. F_1 is a blended function realize transit from the k - ω model in the near wall to the k - ϵ model far from the cylinder surface, which is defined as followed:

$$F_1 = \tanh(\arg_1^4) \quad (7)$$

$$\arg_1 = \min \left[\max \left(\frac{\sqrt{k}}{\beta^* \omega d}, \frac{500\nu}{d^2 \omega} \right), \frac{4\alpha_{\omega 2} k}{CD_{k\omega}^* d^2} \right] \quad (8)$$

where $CD_{k\omega}^* = \max(CD_{k\omega}, 10^{-10})$, in which $CD_{k\omega} = 2\alpha_{\omega 2} \frac{1}{\omega} \frac{\partial k}{\partial x_j} \frac{\partial \omega}{\partial x_j}$. Values of parameters in transport equations can also obtained through $\varphi = F_1 \varphi_1 + (1 - F_1) \varphi_2$, in which φ represents parameters of α, β, γ . The eddy viscosity ν_t can be solved as followed:

$$\nu_t = \frac{a_1 k}{\max(a_1 \omega, b_1 S F_2)} \quad (9)$$

$$F_2 = \tanh(\arg_2^2) \quad (10)$$

$$\arg_2 = \max \left(2 \frac{\sqrt{k}}{\beta^* \omega d}, \frac{500\nu}{d^2 \omega} \right) \quad (11)$$

where d is the distance between the grid point and the cylinder surface. All empirical parameters in equations above can refer to Zhao and Wan (2016) [45].

2.2. Structural governing equations

The flexible cylinder, investigated in this paper, is regarded as a physical model satisfying the assumptions as follows.

- (1) The material is uniform, and all the sections are the same.
- (2) A Euler-Bernoulli bending beam with the axial pretension.
- (3) Ignoring the torsional deformation and axial tensile deformation of the structure.
- (4) The connection between cylinder and both sides of boundary are regarded as simply supported connection.

Crossflow and inline vibrations of the model are calculated through the FEM method. Corresponding structural governing equations in each element are written as followed:

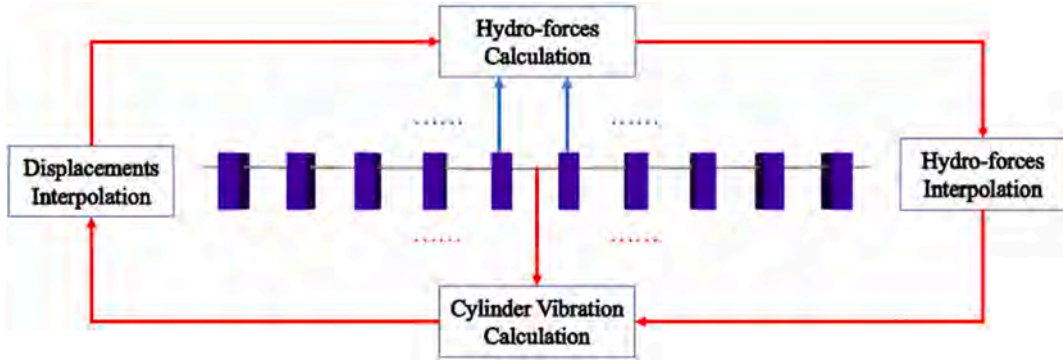


Fig. 1. Schematic diagram of the thick strip theory.

$$EI \frac{\partial^4 x(z,t)}{\partial z^4} - \frac{\partial}{\partial z} \left[T(z) \frac{\partial x(z,t)}{\partial z} \right] + m \frac{\partial^2 x(z,t)}{\partial t^2} + c \frac{\partial x(z,t)}{\partial t} = f_x(z,t) \quad (12)$$

$$EI \frac{\partial^4 y(z,t)}{\partial z^4} - \frac{\partial}{\partial z} \left[T(z) \frac{\partial y(z,t)}{\partial z} \right] + m \frac{\partial^2 y(z,t)}{\partial t^2} + c \frac{\partial y(z,t)}{\partial t} = f_y(z,t) \quad (13)$$

where EI is the bending stiffness, $T(z)$ is the axial tension applied at each element, m is the element mass, c is the damping, $f_x(z,t)$, $f_y(z,t)$ are inline and crossflow hydrodynamic forces acted at each element respectively. Then, the governing equations of the whole system can be written as followed.

$$\mathbf{M}\{\ddot{\mathbf{X}}\} + \mathbf{C}\{\dot{\mathbf{X}}\} + \mathbf{K}\{\mathbf{X}\} = \{\mathbf{F}_{HX}\} \quad (14)$$

$$\mathbf{M}\{\ddot{\mathbf{Y}}\} + \mathbf{C}\{\dot{\mathbf{Y}}\} + \mathbf{K}\{\mathbf{Y}\} = \{\mathbf{F}_{HY}\} \quad (15)$$

where \mathbf{M} , \mathbf{C} , \mathbf{K} are the mass, damping and stiffness matrixes of the system; $\{\mathbf{F}_{HX}\}$, $\{\mathbf{F}_{HY}\}$ are hydrodynamic force vectors in the inline and crossflow directions. Moreover, the Rayleigh damping is applied in present study in order to generate the damping matrix replacing the practical damping, which has been used and validated by Duanmu et al. (2017) [40], Fu et al. (2018) [42] and Deng et al. (2020) [37] in their investigations.

2.3. Thick strip model

Traditional strip theory put forward by Willden et al. (2004) [46] only observes the three-dimensional fluid field through some two-dimensional strips, and the simplification makes the three-dimensional characteristic of the flow field and the axial correlation are neglected. This results in the underestimation of the hydrodynamic forces at complicated flow conditions or cylinders with complex cross-section geometries. Therefore, Bao et al. (2016) [47] proposed the thick strip model. The validity of this model was then verified by Bao et al. (2019) [48] too. Adopting this theory, the CFD code viv3D-FOAM-SJTU solver was developed and verified to be available in predicting VIV responses of a flexible cylinder experiencing the uniform flow and the stepped flow respectively by Deng et al. (2020) [37].

In this paper, all numerical simulations are carried out by the viv3D-FOAM-SJTU solver. Incompressible flow fields in each three-dimensional fluid strip are solved by the PimpleDyMFoam solver in the OpenFOAM. Then, hydrodynamic forces will be transferred as uniformly distributed loads and applied to structural elements using the cubic spline interpolation method. Vibrations of the flexible cylinder in both directions are calculated using the FEM method combined with the Newmark- β algorithm. The calculated vibration displacements will be transferred to boundary points in each fluid strip and update the computational mesh using dynamic grid technique at each time step. The procedure of solution is shown in Fig. 1: in each time step, calculate the hydro-forces according to the deformation of the cylinder of last time step first, and then solve the structural equation with the hydro-forces to obtain the two-dimensional horizontal displacements of the structure elements, which determine the new deformation of the cylinder in the present time step.

3. Simulation setup

3.1. Model setup

Numerical simulations are carried out based on experiments of Lehn (2003) [49] where a smooth flexible cylinder is exposed to the uniform flow as show in Fig. 2, the cylinder is fixedly connected with the top and the bottom boundary. We define x direction is the

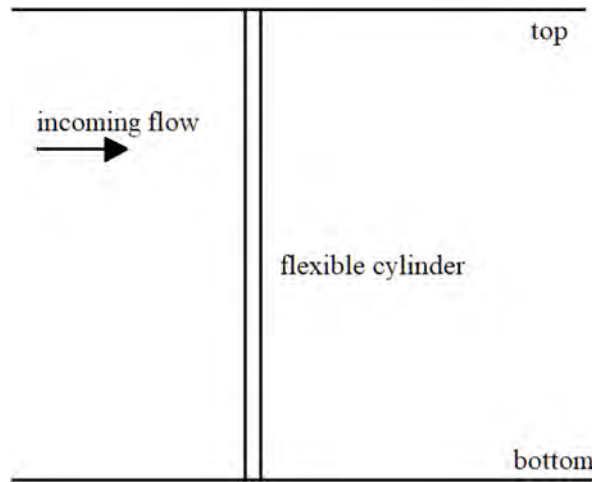


Fig. 2. Side view schematic diagram of the experiment.

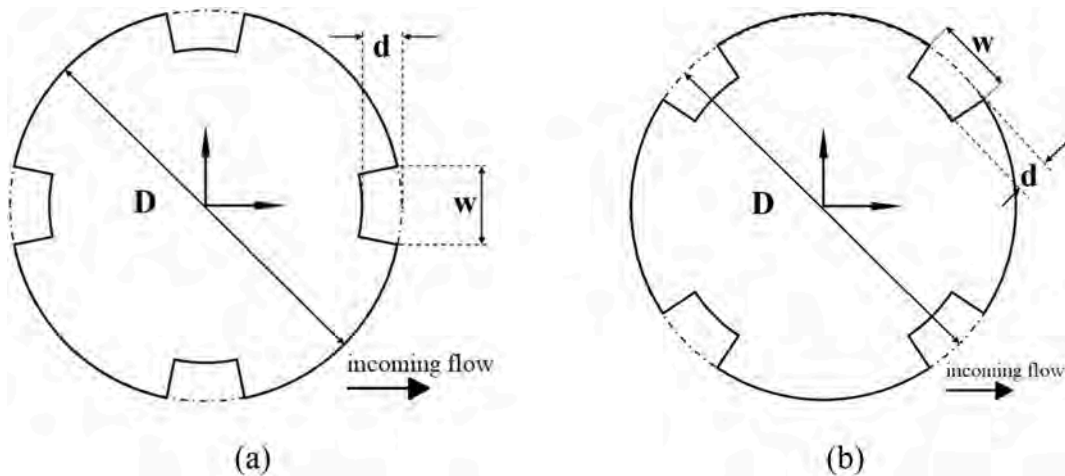


Fig. 3. Schematic diagram of cross-section geometry of the cylinder: (a) Configuration A (phase = 0°); (b) Configuration B (phase = 45°).

Table 1
Main parameters of the cylinder model with spanwise grooves.

	Properties	Values	Unit
Length	L	9.63	m
Diameter	D	0.02	m
Structural stiffness	EI	135.4	N·m ²
Top tension	T	817	N
Mass ratio	m^*	2.23	–
Aspect ratio	L/D	481.5	–
Flow velocity	U	0.2	m/s

same as the flow, and y direction is defined as the horizontal normal direction of x direction, and z direction is the vertical direction normal to both x and y directions. Detailed validations have been conducted among simulations by the viv3D-FOAM-SJTU solver, model experiments and simulations from Wang and Xiao (2016) [50] by Deng et al. (2020) [37].

3.2. Grooves arrangements

Four spanwise grooves with a constant width (w) and three different depths (d , along the radial direction of the cylinder) are applied to the same cylinder model with an interval of 90° at two configurations in present studies to modify the cylinder cross-section

Table 2
Spanwise groove geometries.

	Configuration	Groove width (w)	Groove depth (d)
Case1	A	$0.2D$	$0.08D$
Case2	A	$0.2D$	$0.12D$
Case3	A	$0.2D$	$0.16D$
Case4	B	$0.2D$	$0.08D$
Case5	B	$0.2D$	$0.12D$
Case6	B	$0.2D$	$0.16DD$

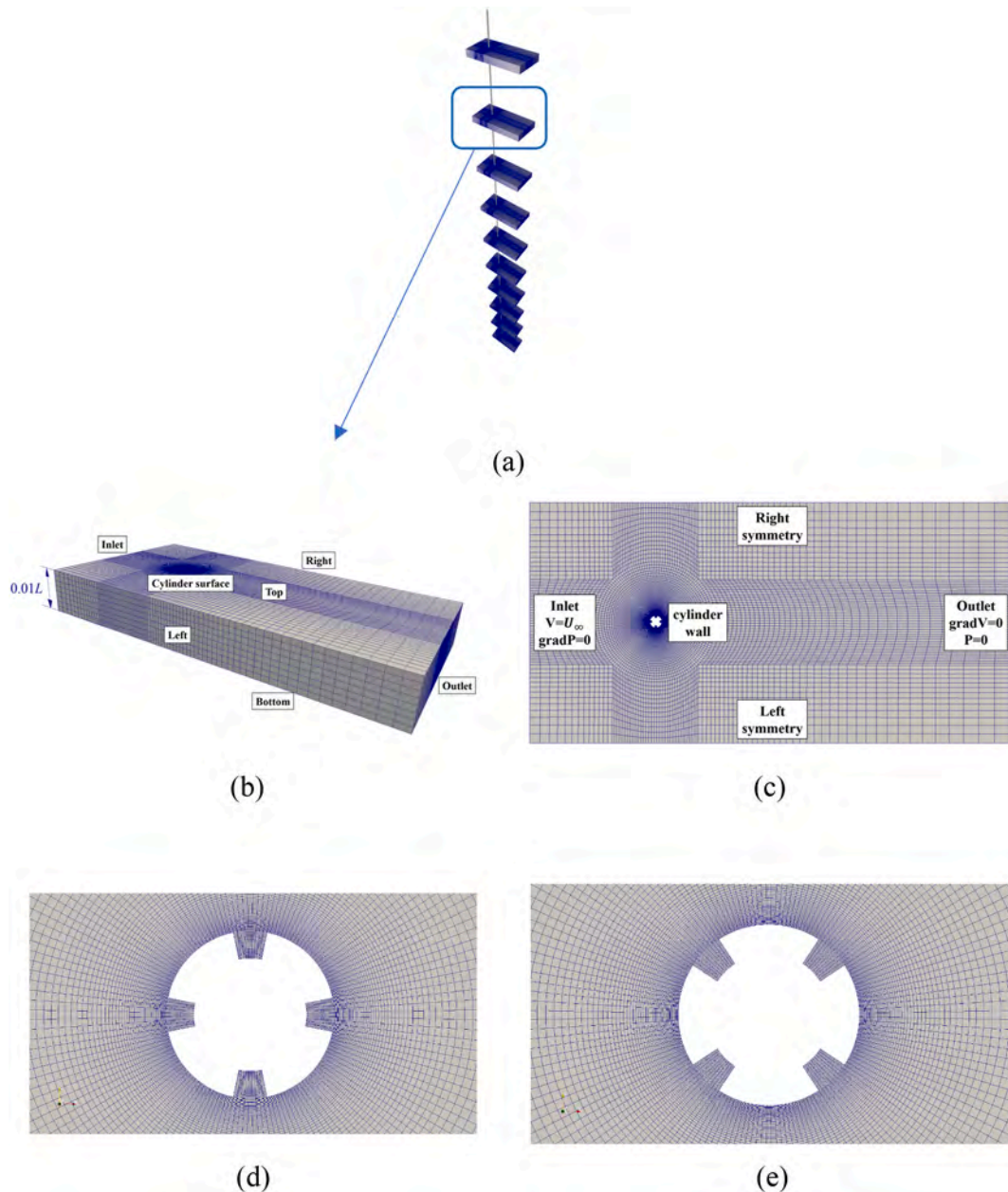


Fig. 4. Computational meshes setup and corresponding boundary conditions: (a) computational model; (b) computational domain of a single fluid strip; (c) boundary conditions; (d) meshes around the cylinder at configuration A; (e) meshes around the cylinder at configuration B.

referring to the simulations of Law and Jaiman (2018) [32] and experiments of Huang (2011) [31]. Schematics of cross-section

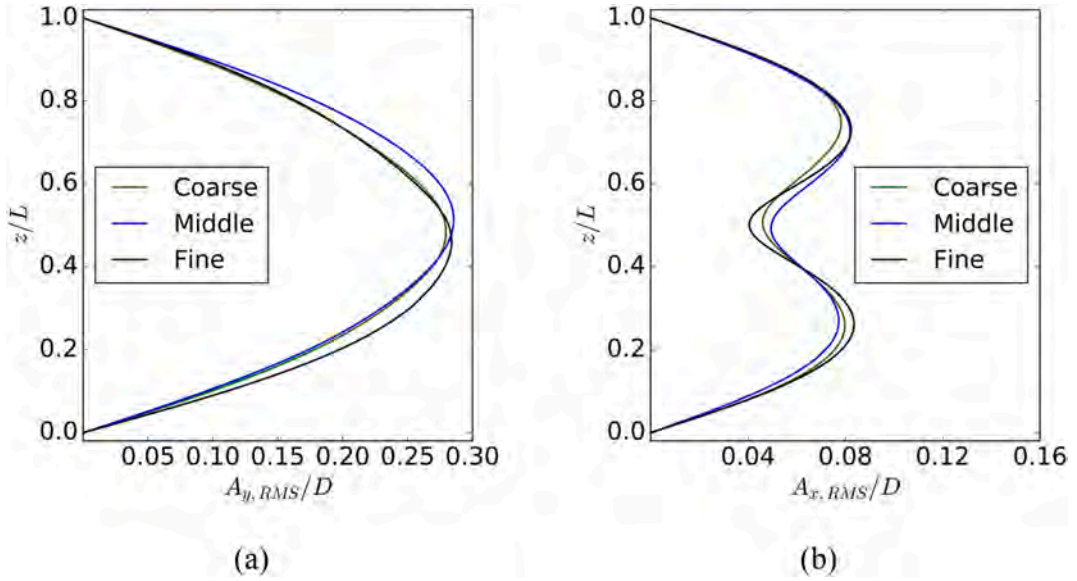


Fig. 5. Comparison of non-dimensional vibration RMS displacement of the cylinder among different mesh resolutions in both directions: (a) crossflow; (b) inline.

geometry of the cylinder model with spanwise grooves are shown in Fig. 3, where $w = 0.2D$ (D is the cylinder diameter) is the width of the groove and $d = 0.16D$ is the depth of the groove. Main parameters of the cylinder model with spanwise grooves and the corresponding flow condition are shown in Table 1, which mainly consult the experiment setup of Lehn (2003) [49]. Six types of spanwise grooves arrangements are mainly studied in this paper with constant groove width and different groove depth at two configurations as shown in Table 2.

3.3. Computational mesh setup

The three-dimensional computational model used in this paper is shown in Fig. 4(a). It can be seen that 10 three-dimensional fluid strips are uniformly distributed along the cylinder span. According to the study of Deng et al. (2020) [37], the three-dimensional vortex shedding feature can be captured when the strip thickness reaches $0.01L$. Therefore, the three-dimensional fluid strip is set to be $40D$ in the inline direction with $-10D \leq x \leq 30D$, $20D$ in the crossflow direction with $-10D \leq y \leq 10D$ and $0.01L$ in the axial direction as shown in Fig. 4(b). In order to obtain physical quantities in the boundary layer of the cylinder surface accurately, meshes near the cylinder surface are refined and guarantee the y^+ near the cylinder surface lower than 3.0 in all simulations. Corresponding boundary conditions are shown in Fig. 4(c): Velocity inlet condition is set at the “Inlet” boundary and pressure outlet condition is adopted in the “Outlet” boundary. Wall condition is applied the “Cylinder surface” boundary, while symmetry condition is for the “Top”, “Bottom”, “Left” and “Right” boundaries. Detailed mesh distributions around the cylinder surface at two configurations are shown in Fig. 4(d) and (e) where the mesh size in grooves is the same as that in the first boundary layer. The flexible cylinder is discretized into 200 finite elements. And in order to ensure the stability and the convergence rate in all simulations, the time step is set to be 0.0005 s to keep the Courant Number not larger than 3.0 during the implicit solution process.

The computational mesh quantity trial is carried out among three mesh resolutions of 2.53 million, 3.76 million and 4.77 million computational cells respectively with the groove width $w = 0.2D$ and the groove depth $d = 0.16D$ at configuration A (Case 1) for all strips collectively, and the meshes of all strips are the same. Fig. 5 presents comparisons of vibration non-dimensional Root Mean Square (RMS) displacements along the cylinder span among three meshes. The RMS displacements can be calculated through Eq [38] and Eq [39].

$$A_{y,RMS}(z) = \sqrt{\sum_{t=t_s}^{t_e} [A_y(z, t)]^2} \quad (16)$$

$$A_{x,RMS}(z) = \sqrt{\sum_{t=t_s}^{t_e} [A_x(z, t) - \bar{A}_x(z)]^2} \quad (17)$$

where $A_{y,RMS}$ is the crossflow RMS displacement along the cylinder span; $A_{x,RMS}$ is the inline RMS displacement along the cylinder span; z is the axial location; t_s is the start time of the chosen interval; t_e is the end time of the chosen interval; $\bar{A}_x(z)$ is the equilibrium position along the cylinder span in the inline direction during the chosen interval.

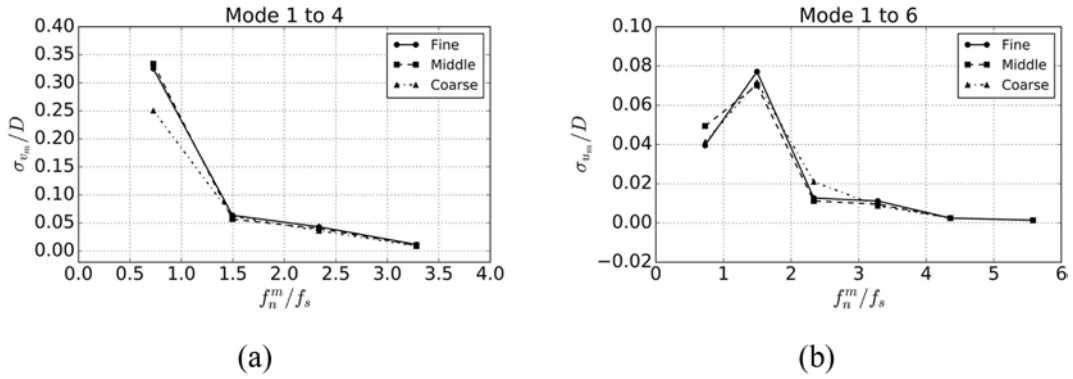


Fig. 6. Comparison of non-dimensional vibration modal weights RMS of the cylinder among different mesh resolutions in both directions: (a) crossflow; (b) inline.

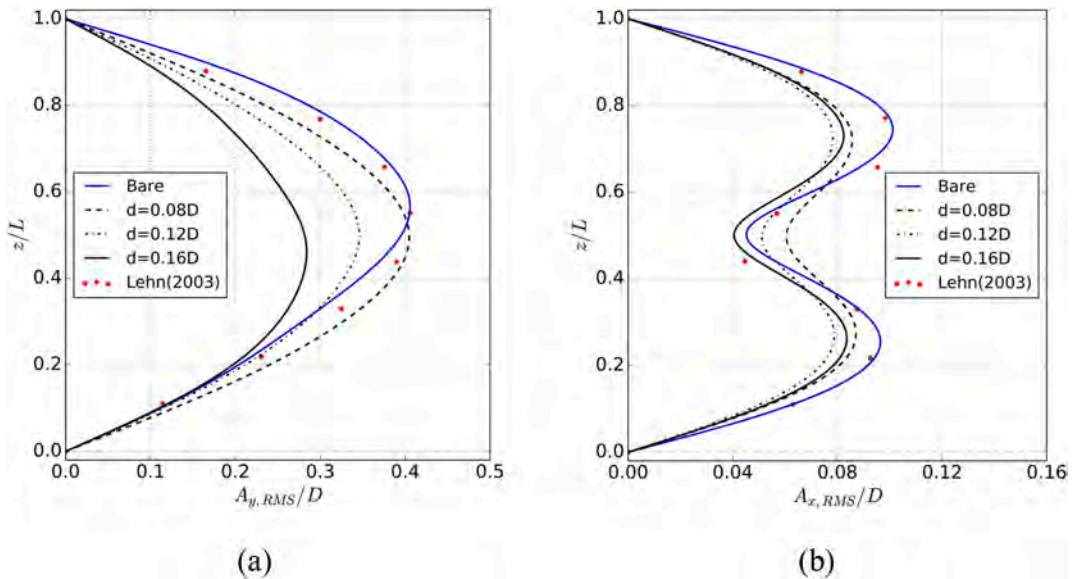


Fig. 7. Comparisons of vibration RMS displacements in both directions with spanwise grooves arranged at configuration A: (a) crossflow; (b) inline.

It can be found from Fig. 5(a) that the maximum crossflow RMS displacement reaches around $0.28D$ for the middle and fine mesh, while it only reaches around $0.27D$ for the coarse mesh condition. The axial location corresponding to the maximum crossflow RMS displacement is around $0.5L$ and the cylinder presents the first mode shape in all mesh resolutions. In the inline direction, the RMS displacement presents the second mode shape in all simulations. Two vibration peaks around $0.08D$ are captured at non-dimensional axial locations around $z/L = 0.25$ and $z/L = 0.75$ along the cylinder. Although, comparatively large computational errors of RMS amplitude can be found between the coarse mesh and middle mesh at around $z/L = 0.75$, the dominant vibration features are well captured. Similar errors can also be found between the middle mesh and the fine mesh at around $z/L = 0.5$ and $z/L = 0.25$. In general, results of crossflow and inline RMS vibration displacements are in good agreement among three mesh resolutions.

The modal decomposition method, which has been proved to be useful in analyzing vibration modal features of the flexible cylinder in both experiments and numerical simulations by Chaplin et al. (2005) [44] and Fu et al. (2018) [42], is adopted in the present study. The time-history vibration displacements along the cylinder axial direction can be divided into a series of modal shapes at each time step as followed:

$$\varphi_n(z) = \sin\left(\frac{n\pi}{L}z\right) \tag{18}$$

$$x(z, t) = \sum_{n=1}^N u_n(t) \cdot \varphi_n(z) \tag{19}$$

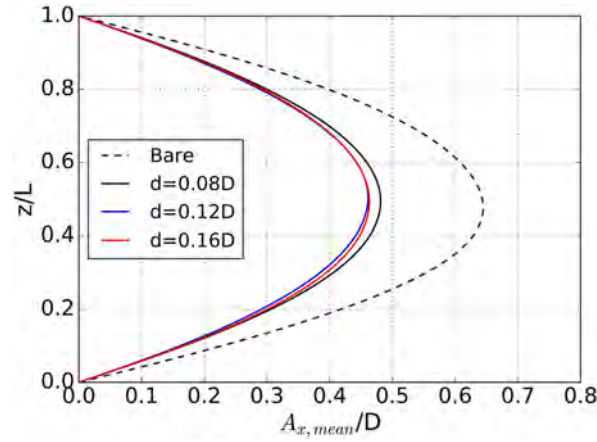


Fig. 8. Comparisons of inline mean vibration displacements with spanwise grooves arranged at configuration A.

Table 3

The main parameters of the crossflow vibration modal decomposition results at configuration A.

Case	Groove depth	Dominant vibration frequency	Amplitude of dominant vibration frequency
Smooth cylinder	0	1.684 Hz	0.00500
Case 1	0.08D	1.498 Hz	0.00445
Case 2	0.12D	1.504 Hz	0.00385
Case 3	0.16D	1.496 Hz	0.00245

$$y(z, t) = \sum_{n=1}^N v_n(t) \cdot \varphi_n(z) \quad (20)$$

where z is the axial location of the cylinder nodes; L is the length of the cylinder; $x(z, t)$ is the inline vibration displacement; $y(z, t)$ is the crossflow vibration displacement; $u_n(t)$ is the time-history modal weight in the inline direction for the n th mode; $v_n(t)$ is the time-history modal weight in the crossflow direction for the n th mode and N is the maximum mode number determined by the element number of the cylinder model. The RMS modal weights in both directions can be calculated using Eq [38] and Eq [39]. The Strouhal frequency is adopted to normalize the natural frequency of the cylinder, which can be written as Eq [12].

$$f_s = \frac{U \cdot St}{D} \quad (21)$$

where $St = 0.2$ is the Strouhal number used in the present study.

The dominant vibration mode keeps the first mode in the crossflow direction and the second mode in the inline direction among three mesh resolutions as shown in Fig. 6. Obvious deviations can be found between the coarse mesh and the fine mesh at the first modal weight RMS value in the both directions and the third modal weight RMS value in the inline direction, which determines that the coarse mesh cannot be adopted. Similar deviation can also be found at the second modal between the middle mesh and the fine mesh in the inline direction, which also means that the result of middle mesh is not accurate enough. However, the variation tendencies of modal weight RMS values in both directions are in good agreement among three mesh resolutions. Considering the comparisons above and the capture of three-dimensional vortex structures in the wake flow, the fine mesh with more-refined axial mesh distribution is chosen for following simulations.

Table 4

The main parameters of the inline vibration modal decomposition results at configuration A.

Case	Groove depth	Dominant vibration frequency	Amplitude of dominant vibration frequency
Smooth cylinder	0	3.4 Hz	0.00146
Case 1	0.08D	3.11 Hz	0.00092
Case 2	0.12D	3.17 Hz	0.00070
Case 3	0.16D	3.19 Hz	0.00095

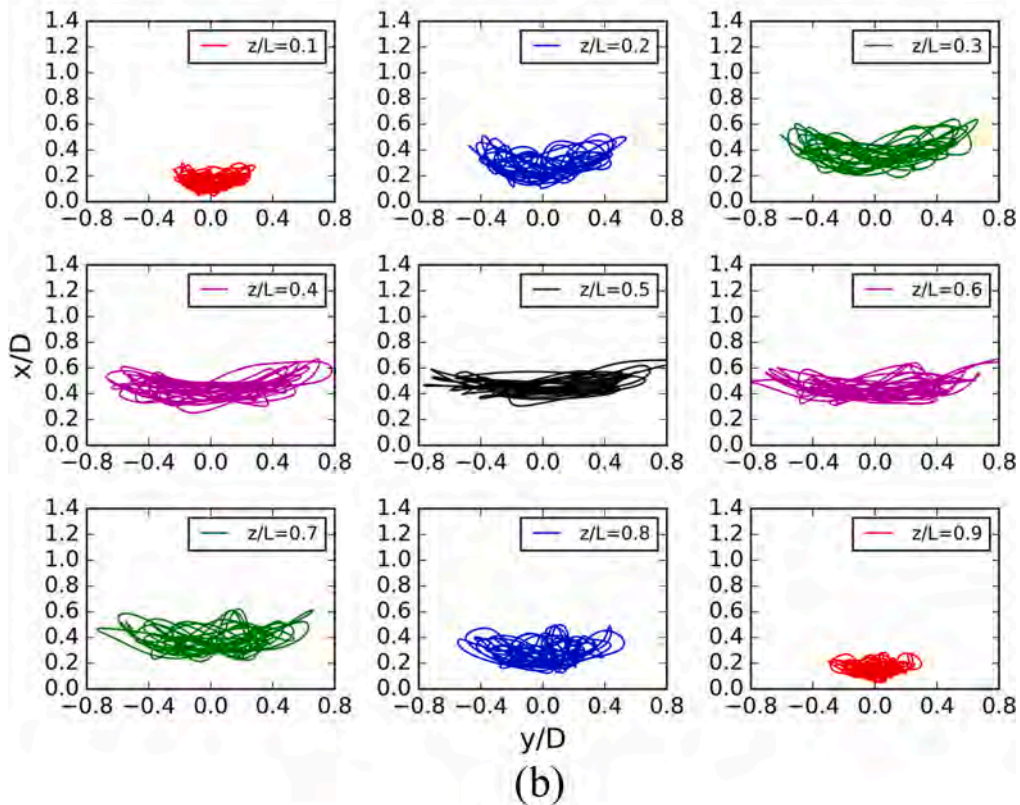
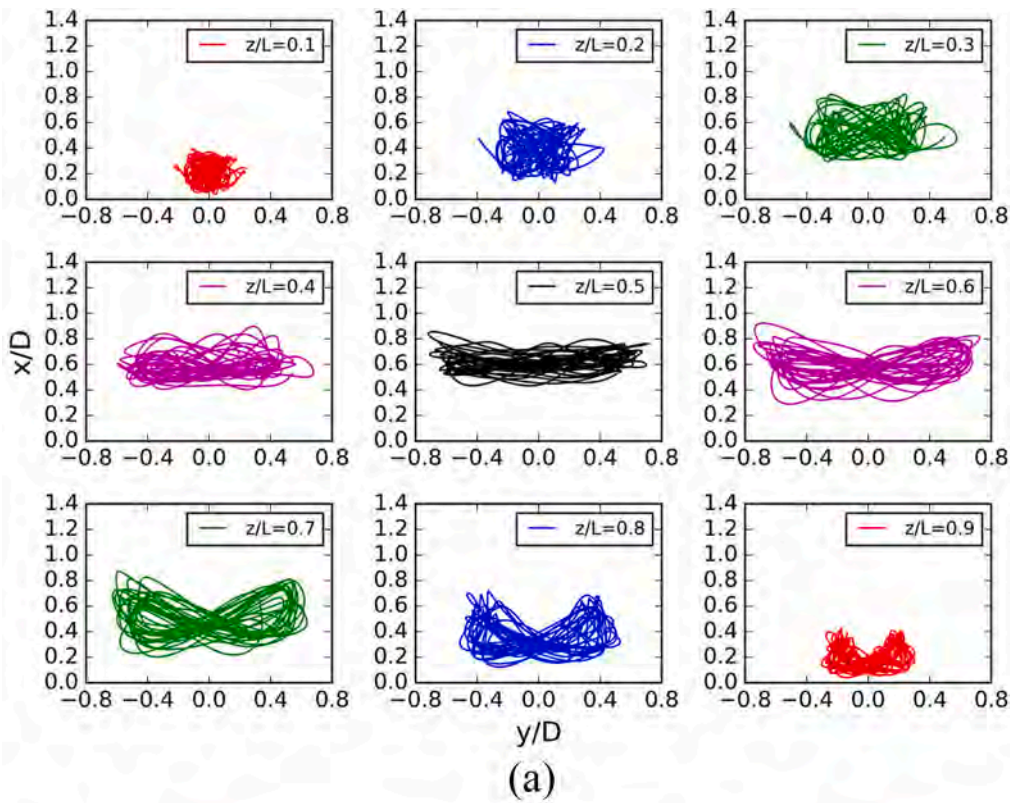


Fig. 9. Vibration trajectories along the cylinder span among smooth cylinder and cylinders with different groove depths at configuration A: (a) smooth cylinder; (b) Case1 ($d = 0.08D$); (c) Case2 ($d = 0.12D$); (d) Case3 ($d = 0.16D$).

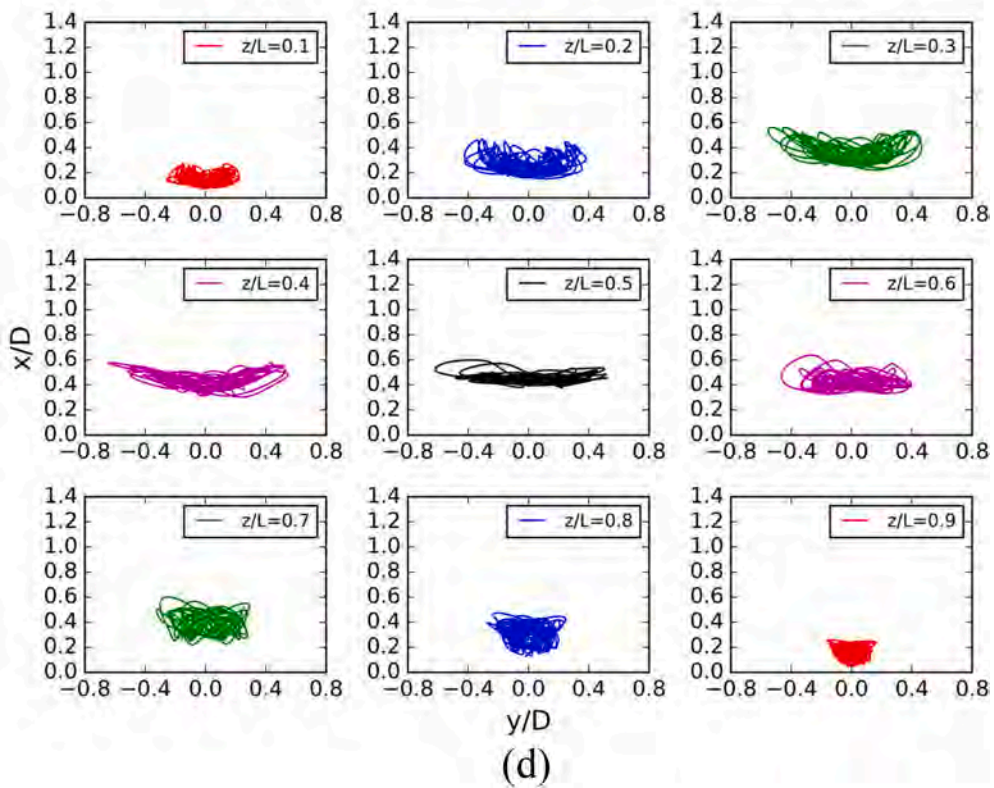
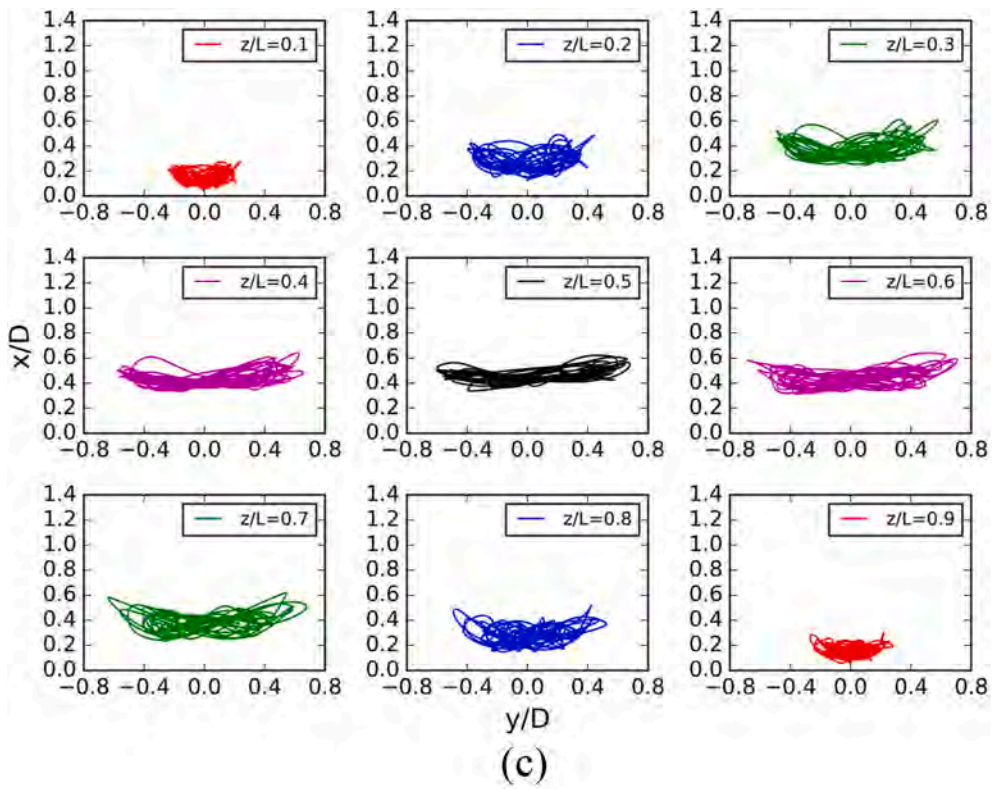


Fig. 9. (continued).

4. Results and discussions

4.1. Effects of spanwise grooves on VIV responses at configuration A

Comparisons of crossflow and inline vibration RMS displacements among experiments of Lehn (2003) [49], smooth cylinder (Deng et al., 2020) and cylinders with different depths of spanwise grooves at configuration A (Case1, Case2 and Case3) are shown in Fig. 7. It can be found in Fig. 7(a) that the maximum crossflow RMS displacement reaches around $0.41D$ with its corresponding axial locations decreases to around $0.5L$ compared with the smooth cylinder condition when the depth of spanwise grooves is $0.08D$ (Case1), which presents none suppression effect on crossflow vibration. With the increase of the groove depth (d) from $0.08D$ to $0.16D$, the maximum crossflow RMS displacement decreases to around $0.35D$ (Case2) and $0.28D$ (Case3) respectively, while the corresponding axial locations are barely changed. The inline suppression effects from spanwise grooves are not sensitive to the groove depth from Fig. 7(b). The maximum inline vibration RMS displacements decrease to around $0.08D$ with its axial locations at around $0.25L$ and $0.75L$ among three different groove depths. It can also be found from comparisons of inline mean vibration displacement in Fig. 8 that the maximum

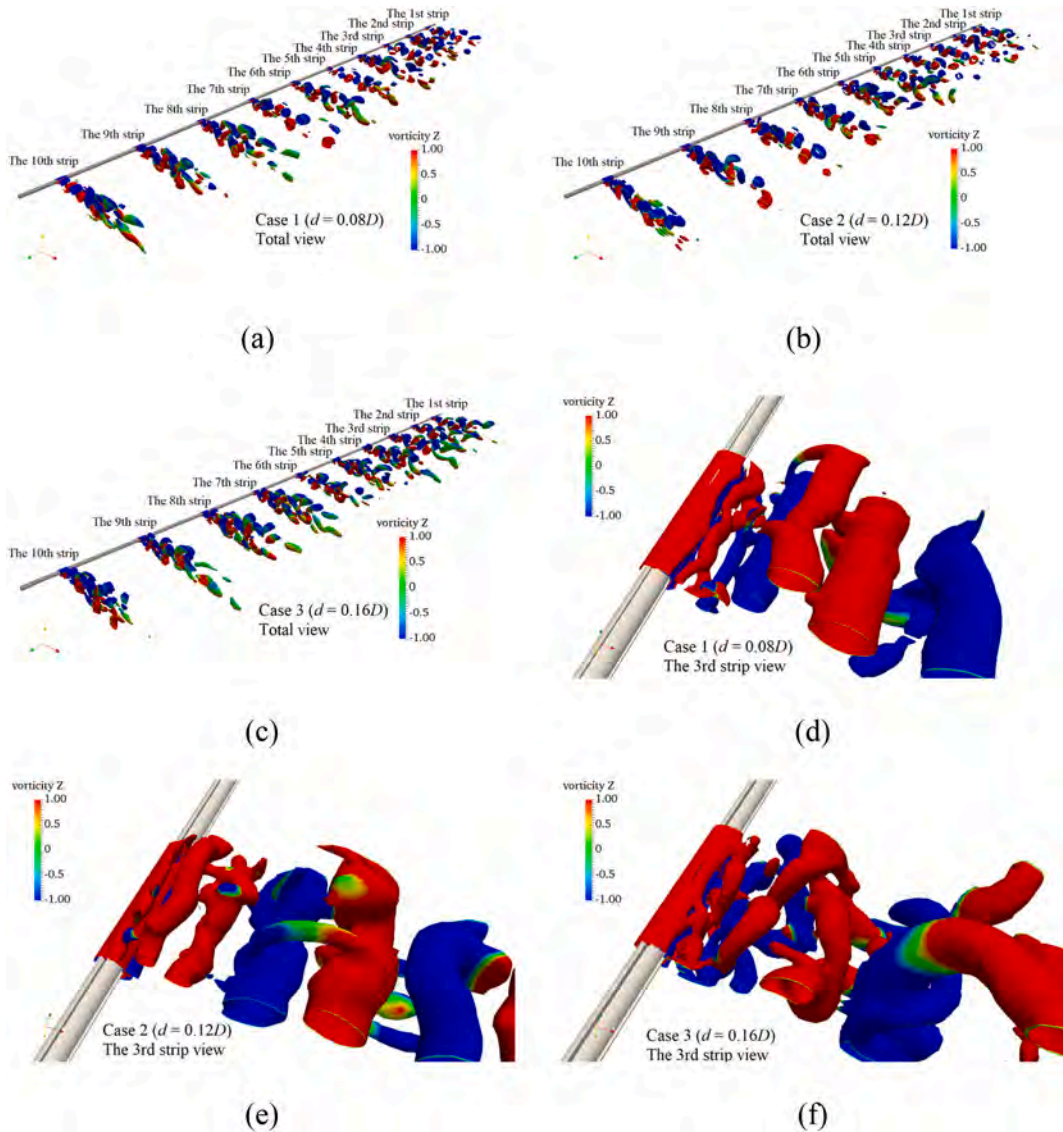


Fig. 10. Instantaneous vortex structures through the Q criterion ($Q = 5$) of the total cylinder and three fluid strips at $t = 47$ s among cylinders with different groove depths at configuration A: (a) Case 1 ($d = 0.08D$), total view; (b) Case 2 ($d = 0.12D$), total view; (c) Case 3 ($d = 0.16D$), total view; (d) Case 1 ($d = 0.08D$), the 3rd strip; (e) Case 2 ($d = 0.12D$), the 3rd strip; (f) Case 3 ($d = 0.16D$), the 3rd strip; (g) Case 1 ($d = 0.08D$), the 5th strip; (h) Case 2 ($d = 0.12D$), the 5th strip; (i) Case 3 ($d = 0.16D$), the 5th strip; (j) Case 1 ($d = 0.08D$), the 7th strip; (k) Case 2 ($d = 0.12D$), the 7th strip; (l) Case 3 ($d = 0.16D$), the 7th strip.

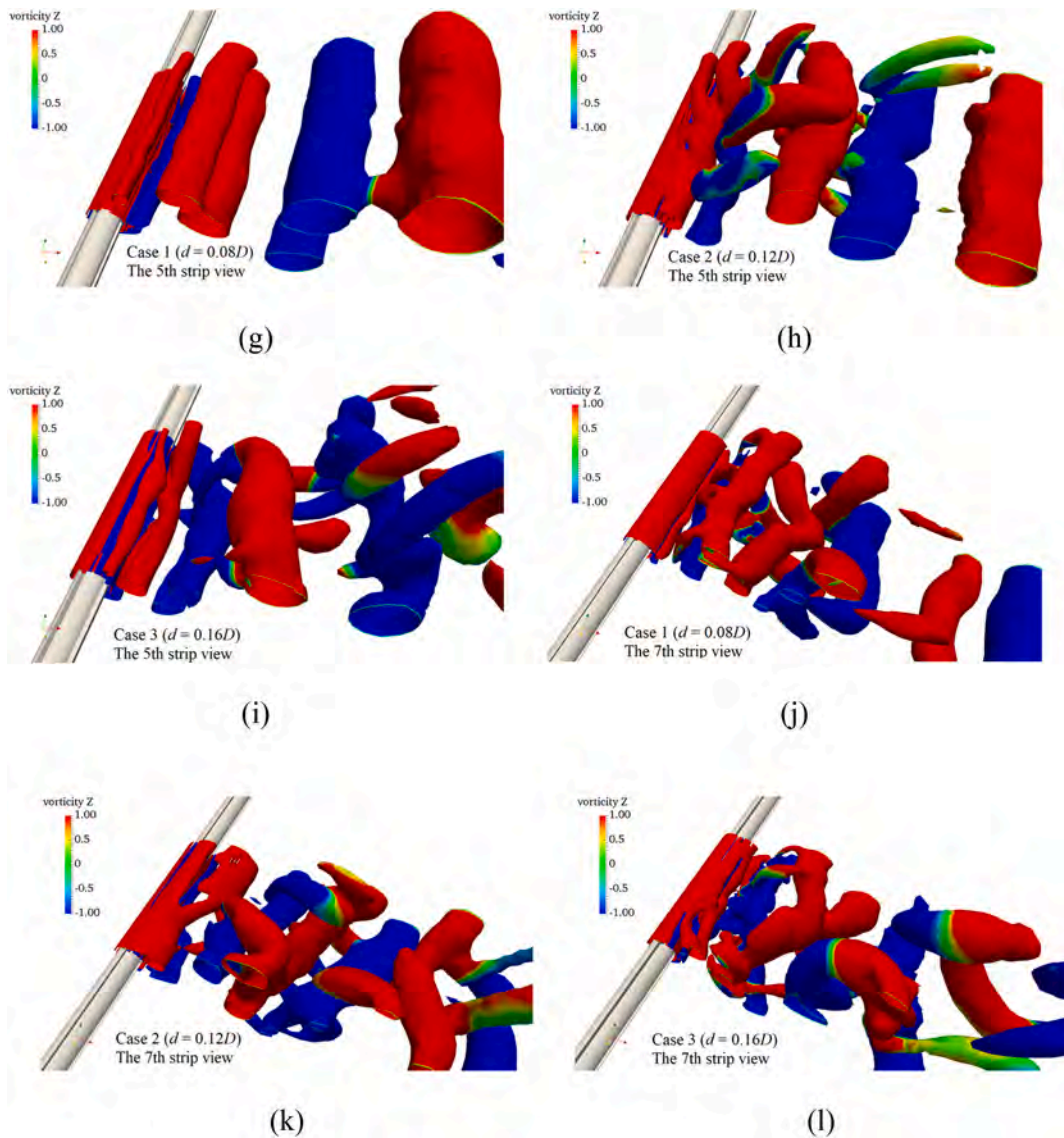


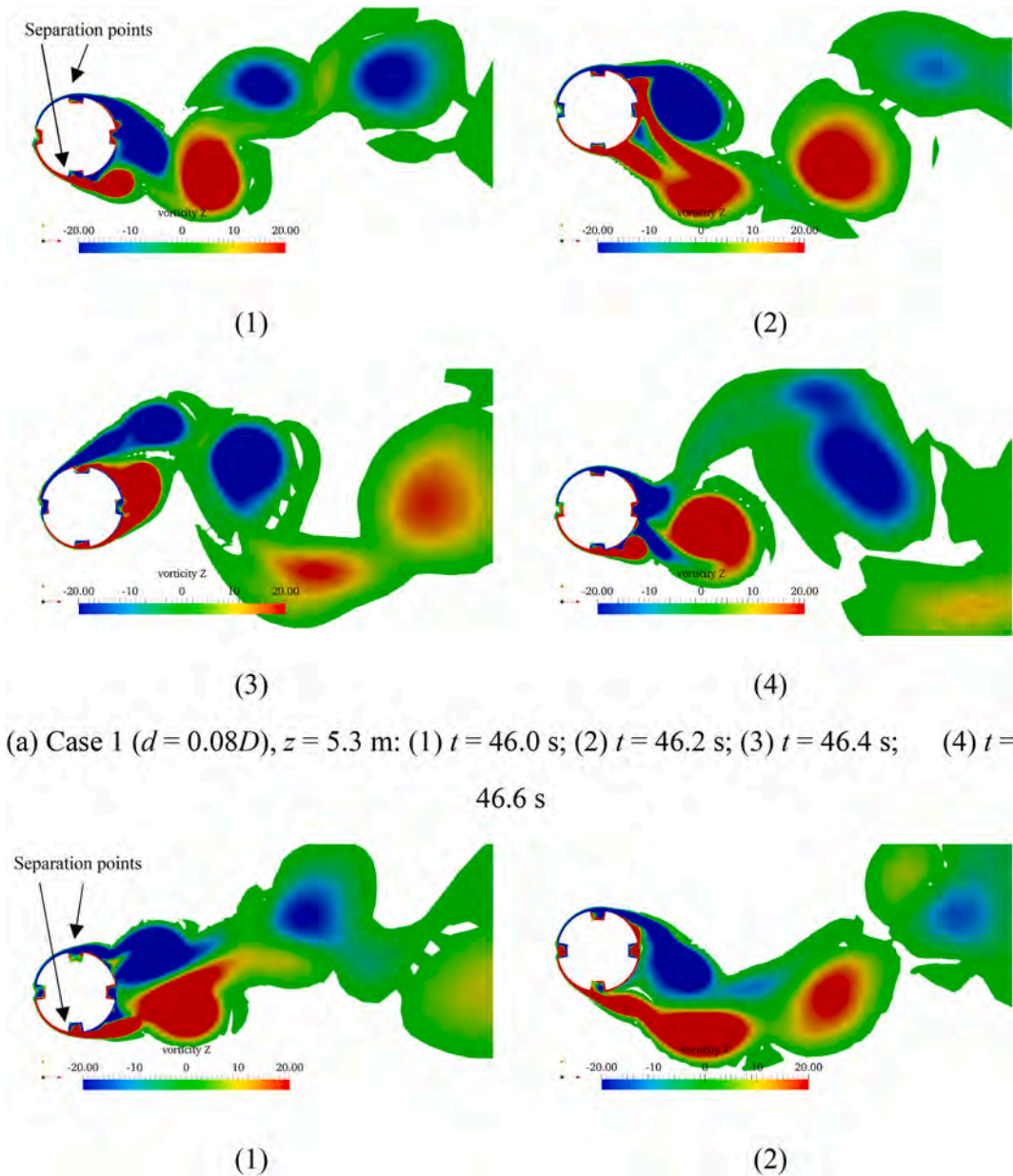
Fig. 10. (continued).

inline mean displacement decreases from $0.65D$ to around $0.46D$ under the suppression effects of spanwise grooves. With the increase of the groove depth from $0.08D$ to $0.16D$, the maximum inline mean vibration displacement decreases from $0.48D$ (Case1) to around $0.45D$ (Case3), which also illustrate that the variation of the groove depth plays negligible effects on VIV suppression in the inline direction.

The modal decomposition method as shown in Eq [30]-Eq [7] are adopted to obtain vibration modal weights in both directions. The Fast Fourier Transform (FFT) method is used to get the dominant vibration frequency of the cylinder.

Comparisons of crossflow vibration modal decomposition results and corresponding power spectral density (PSD) among the smooth cylinder and cylinders with different groove depths at configuration A are shown in Fig. 17 of appendix. According to the time-history modal weights among different vibration modes, we found that the first mode keeps the dominant vibration mode in all simulations. The main parameters of results are listed in Table 3. The dominant vibration frequency corresponding to the dominant vibration mode of the smooth cylinder presents around 1.684 Hz in the crossflow direction. Meanwhile, the crossflow dominant vibration frequencies are 1.498 Hz, 1.504 Hz and 1.496 Hz respectively when the groove depths increase from $0.08D$ (Case1) to $0.16D$ (Case3), which illustrate that the spanwise grooves can effectively reduce the dominant vibration frequency and the reduction is not sensitive to the groove depth at configuration A. On the other hand, the comparison of the amplitude of dominant vibration frequency indicates that it decreases with the groove depth.

Comparisons of inline vibration modal decomposition results and corresponding PSD results among smooth cylinder and cylinders with different groove depths at configuration A are shown in Fig. 18 of appendix. The inline vibration presents the second dominant

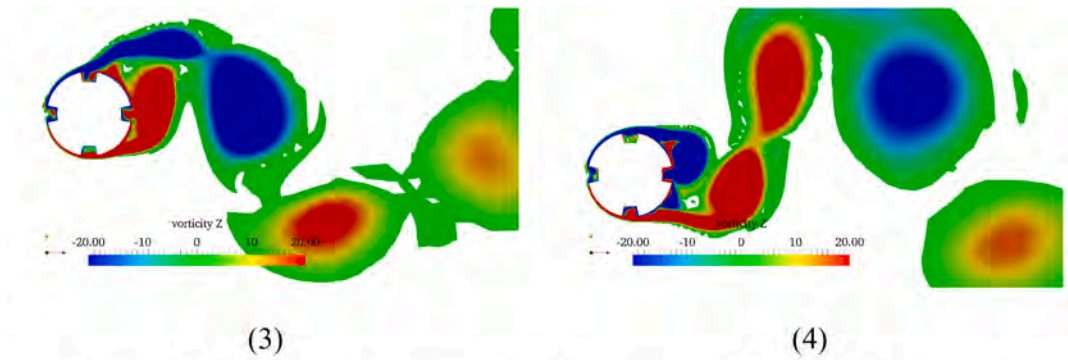


(a) Case 1 ($d = 0.08D$), $z = 5.3$ m: (1) $t = 46.0$ s; (2) $t = 46.2$ s; (3) $t = 46.4$ s; (4) $t = 46.6$ s

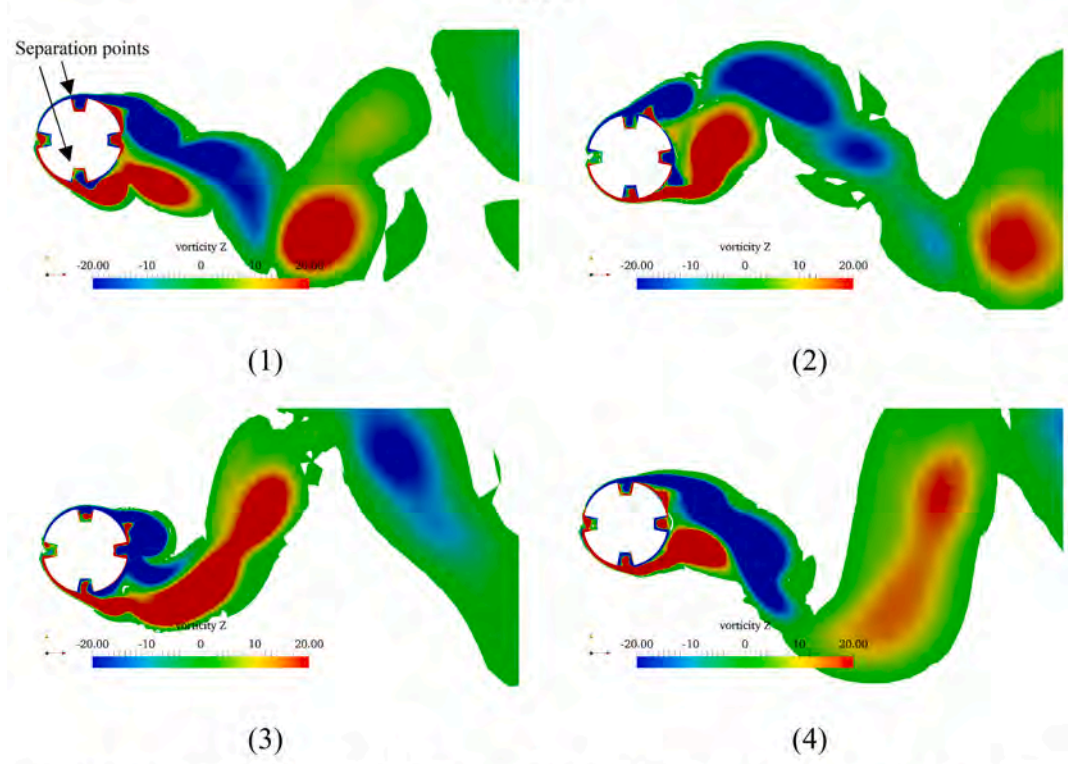
Fig. 11. Instantaneous vorticity- z ($\omega_z = \frac{dv}{dx} - \frac{du}{dy}$) contours at the same axial location along the cylinder with different groove depths at configuration A 4.2 Effects of spanwise grooves on VIV responses at configuration B.

vibration mode in all simulations. The main parameters of results are listed in Table 4. The dominant vibration frequency corresponding to the dominant vibration mode of the smooth cylinder presents around 3.4 Hz in the inline direction, while the inline dominant vibration frequency reduces to 3.11 Hz (Case1), 3.17 Hz (Case2) and 3.19 Hz (Case3) respectively with the increase of the groove depth. Contributing to the suppression effects of spanwise grooves at configuration A, dominant vibration frequencies reduce at around 10.7 % and 7.1 % in the crossflow and inline directions respectively. While the variation of the groove depths presents little suppression effects on vibration frequency responses of the flexible cylinder. In addition, in cases with grooves, the amplitude of dominant vibration frequency decrease obviously when compared with the smooth cylinder, but it is not significantly correlated with the groove depth in the inline direction.

Comparisons of vibration trajectories at nine axial locations from $z/L = 0.1$ to $z/L = 0.9$ along the cylinder span among the smooth cylinder and cylinders with different groove depths at configuration A are shown in Fig. 9. It can be found in Fig. 9(a) that the vibration trajectory presents an approximate rectangle shape at the lower part of the cylinder from $z/L = 0.1$ to $z/L = 0.3$. The vibration shape



(b) Case 2 ($d = 0.12D$), $z = 5.3$ m: (1) $t = 46.0$ s; (2) $t = 46.2$ s; (3) $t = 46.4$ s; (4) $t = 46.6$ s



(c) Case 3 ($d = 0.16D$), $z = 5.3$ m: (1) $t = 46.0$ s; (2) $t = 46.2$ s; (3) $t = 46.4$ s; (4) $t = 46.6$ s

Fig. 11. (continued).

changes to the “long strip” shape at the middle part of the cylinder where the inline vibration amplitude around its equilibrium position reaches the minimum and the corresponding crossflow vibration amplitude reaches its maximum, which is consistent with the dominant first vibration mode of the cylinder. While the obvious “8” shape of vibration trajectory can be observed at $z/L = 0.7$, and the trajectory shape tends to become the approximate “V” shape at $z/L = 0.8$ and 0.9 . Contributing to the effects of spanwise grooves at configuration A, the maximum inline vibration amplitude decreases from around $0.9D$ of the smooth cylinder to around $0.65D$ of the cylinder with the groove depth $d = 0.16D$ (Case3), and the maximum crossflow vibration amplitude decreases from around $0.8D$ to around $0.7D$ as shown in Fig. 9. Meanwhile, the “8” shape of vibration trajectory disappears and the “long strip” shape of vibration trajectory dominates the vibration trajectory of the cylinder, though the approximate rectangle shape can still be observed at $z/L = 0.1$ from Fig. 9(c) and $z/L = 0.7, 0.8$ and 0.9 from Fig. 9(d). Moreover, the trajectory width in the inline directions becomes smaller than

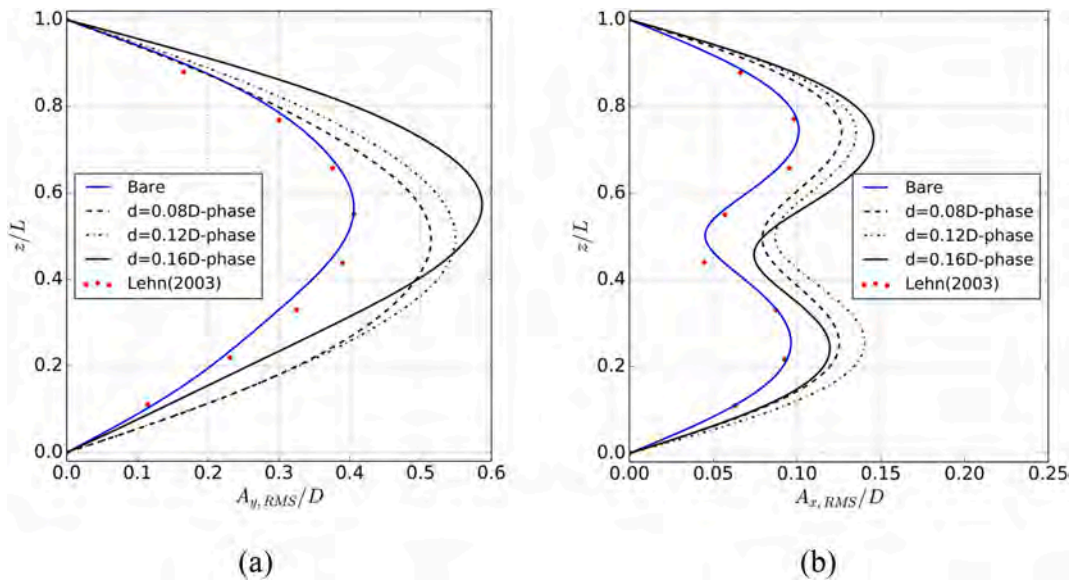


Fig. 12. Comparisons of vibration RMS displacements in both directions with spanwise grooves arranged at configuration B: (a)crossflow; (b)inline.

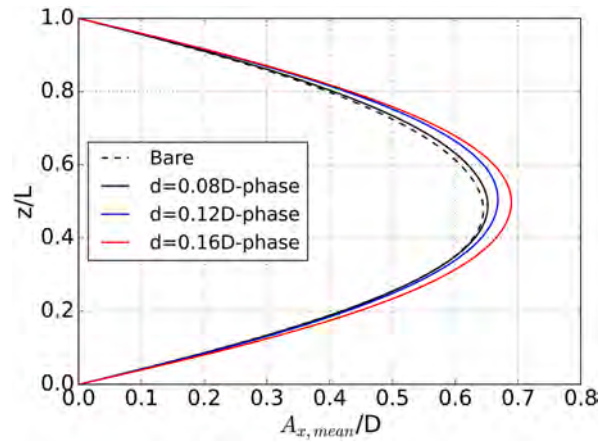


Fig. 13. Comparisons of inline mean vibration displacements with spanwise grooves arranged at configuration B.

Table 5

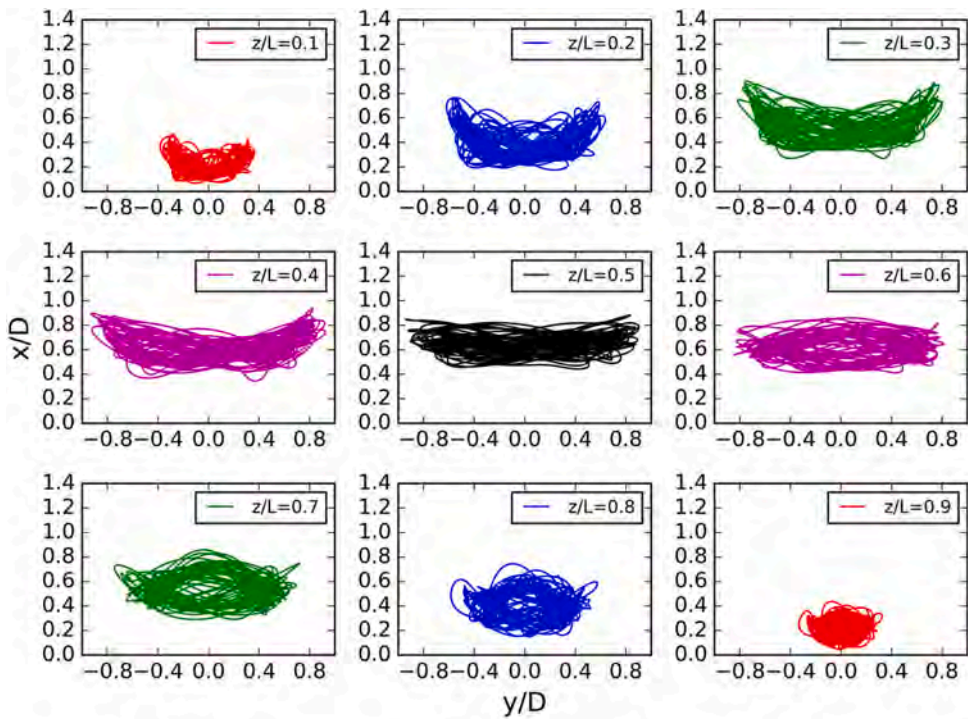
The main parameters of the crossflow vibration modal decomposition results at configuration B.

Case	Groove depth	Dominant vibration frequency	Amplitude of dominant vibration frequency
Smooth cylinder	0	1.684 Hz	0.00500
Case 1	0.08D	1.697 Hz	0.00633
Case 2	0.12D	1.696 Hz	0.00681
Case 3	0.16D	1.702 Hz	0.00756

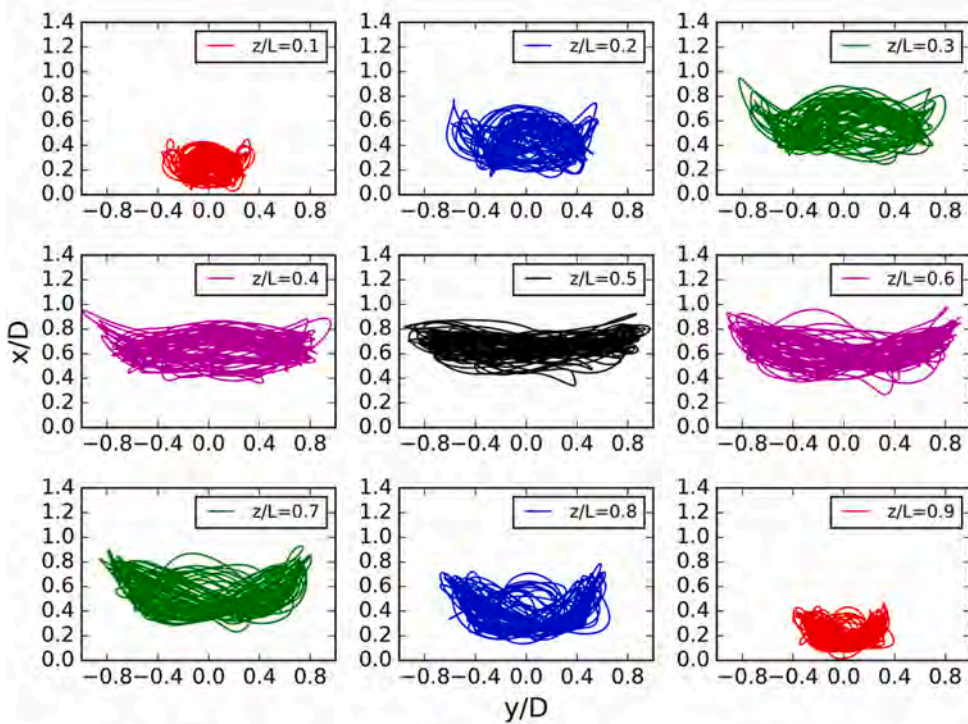
Table 6

The main parameters of the inline vibration modal decomposition results at configuration B.

Case	Groove depth	Dominant vibration frequency	Amplitude of dominant vibration frequency
Smooth cylinder	0	3.4 Hz	0.00146
Case 1	0.08D	3.452 Hz	0.00094
Case 2	0.12D	3.437 Hz	0.00143
Case 3	0.16D	3.402 Hz	0.00136



(a)



(b)

Fig. 14. Vibration trajectories along the cylinder span among cylinders with different groove depths at configuration B: (a) Case4 ($d = 0.08D$); (b) Case5 ($d = 0.12D$); (c) Case6 ($d = 0.16D$).

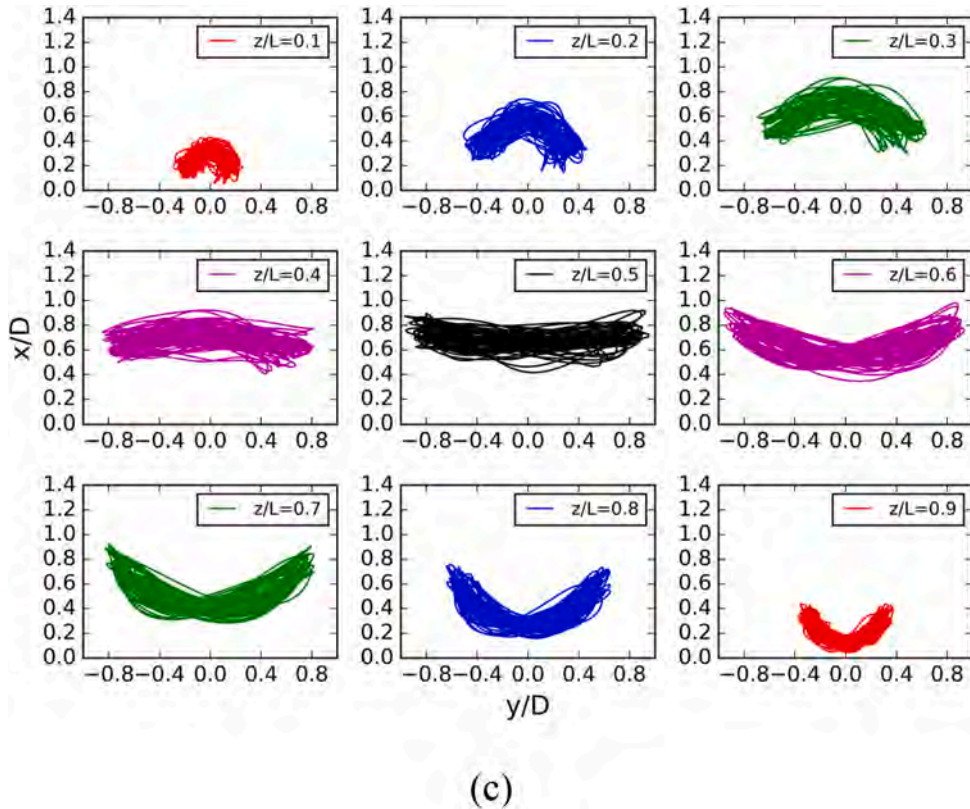


Fig. 14. (continued).

that of the smooth cylinder at the same axial locations with the suppression effects of spanwise grooves at configuration A.

Instantaneous iso-surface of Q -criterion ($Q = 5$) are adopted to illustrate the flow characteristics of the cylinder at $t = 47$ s colored by vorticity- z as shown in Fig. 10. The three-dimensional vortex shedding phenomenon can be obviously observed in Fig. 10(a), (b) and (c) where twisty shape of vortices can be found in all fluid strips, though the approximate cylindrical shape of vortices can still be found in the flow fields at the fourth fluid strip in Fig. 10(a) and the third fluid strip in Fig. 10(b). Corresponding detailed vortex structures around the cylinder at three fluid strips, including the 3rd strip, the 5th strip and the 7th strip, where large crossflow vibration and inline deformation happens as shown in Fig. 10. It can be found in Fig. 10(g) that a cylindrical vortex has been shed from the middle cylinder and presents an approximate wavy shape where inline vibration reaches its stagnation point when the groove depth is $0.08D$ (Case1). While vortices shed from the 3rd and the 7th strip present more obvious twisty characteristics that leads to the generation of small vortices near the cylinder surface and the disordered distribution of vortices far behind the cylinder. When the groove depth increases to $0.12D$ (Case2), the wavy shapes of vortices are more obvious observed. And the vortex shedding positions vary along the axial direction of the cylinder especially as shown in Fig. 10(e) (h) and (k), which strengthens the twisty feature of vortices shed from the cylinder. Therefore, wake flow in Case2 is more disordered than that of Case1. Moreover, discontinuous vortex shedding phenomenon along the axial direction can be observed in the 7th strip in Fig. 10(k). It can be observed that a discrete vortex at the upper part of the fluid strip sheds from the cylinder with its lower part connected with the un-shed vortex. With the evolution of the wake flow, the upper part of the vortex will move away with the flow and the lower part will then sheds from the cylinder that leads to the generation of the curved strip vortex. Vortex becomes discrete before it sheds from the cylinder surface when the groove depth reaches $0.16D$ (Case3) as shown in Fig. 10(f) (i) and (l). Discrete small vortices in the lower and the upper positions of the fluid strip will shed from the cylinder surface firstly, with its corresponding upper and lower parts connected to the vortex attached to cylinder surface, followed by the small vortices in the middle position, which leads to the generation of more small curved strip vortices in the wake flow especially as shown in Fig. 10(f). It can be found that vortex structures become more discrete and disordered with the increase of the groove depth.

In order to visualize the vortex evolution process, the instantaneous vorticity- z (ω_z) contours at $z = 5.3$ m from $t = 46$ s to $t = 46.6$ s among cylinders with different groove depths at configuration A are shown in Fig. 11. It can be found that the separation points on the cylinder surface move to the left edges of the upper and lower grooves as shown in Figs. 11(a-1) where a positive vortex sheds from the cylinder at the left edge of the lower groove, while similar phenomena can also be observed in Figs. 11(b-2) and Fig. 11(c-1). Due to the

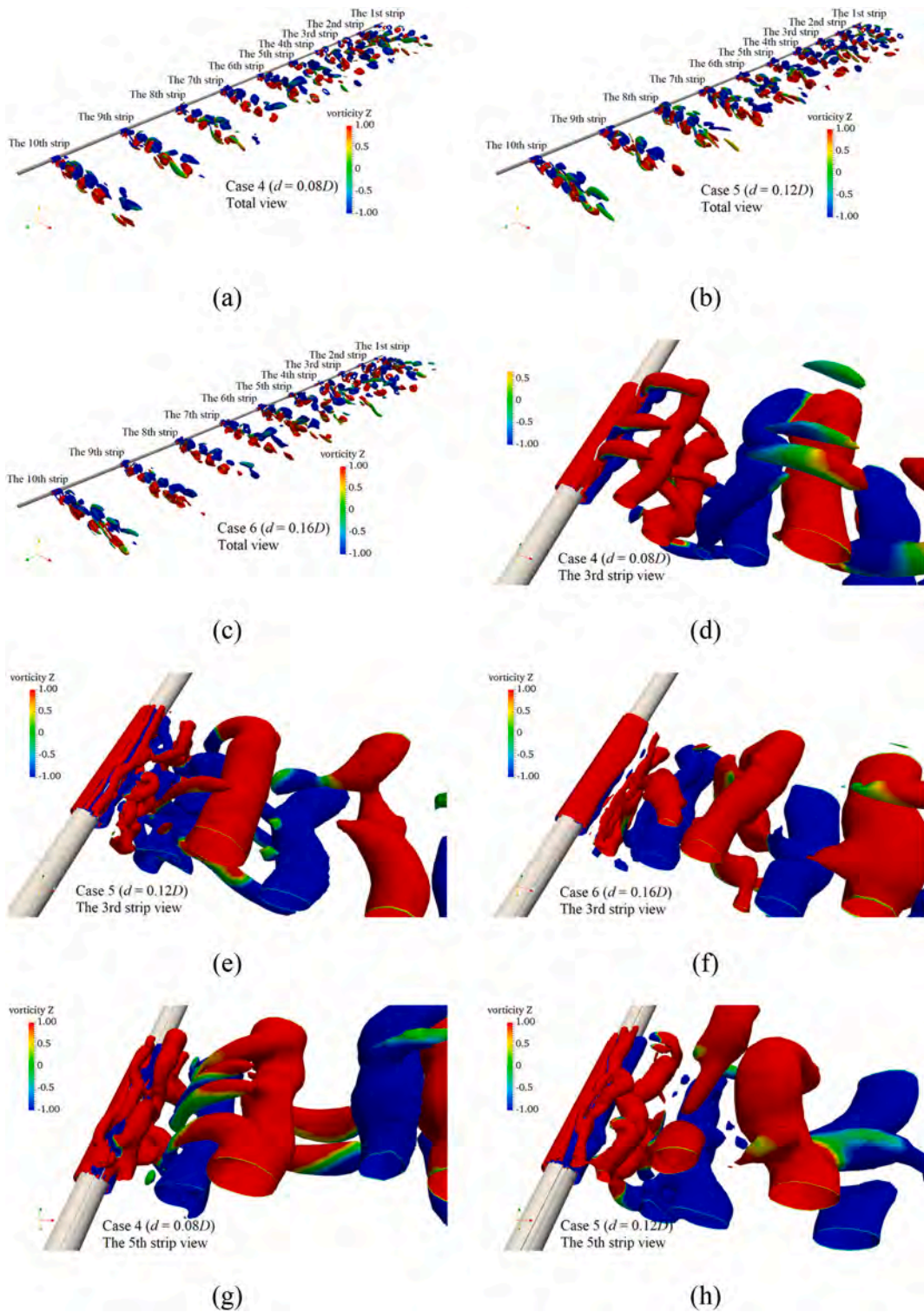


Fig. 15. Instantaneous vortex structures through the Q criterion ($Q = 5$) of the total cylinder and three fluid strips at $t = 47$ s among cylinders with different groove depths at configuration B: (a) Case4 ($d = 0.08D$), total view; (b) Case5 ($d = 0.12D$), total view; (c) Case6 ($d = 0.16D$), total view; (d) Case4 ($d = 0.08D$), the 3rd strip; (e) Case5 ($d = 0.12D$), the 3rd strip; (f) Case6 ($d = 0.16D$), the 3rd strip; (g) Case4 ($d = 0.08D$), the 5th strip; (h) Case5 ($d = 0.12D$), the 5th strip; (i) Case6 ($d = 0.16D$), the 5th strip; (j) Case4 ($d = 0.08D$), the 7th strip; (k) Case5 ($d = 0.12D$), the 7th strip; (l) Case6 ($d = 0.16D$), the 7th strip.

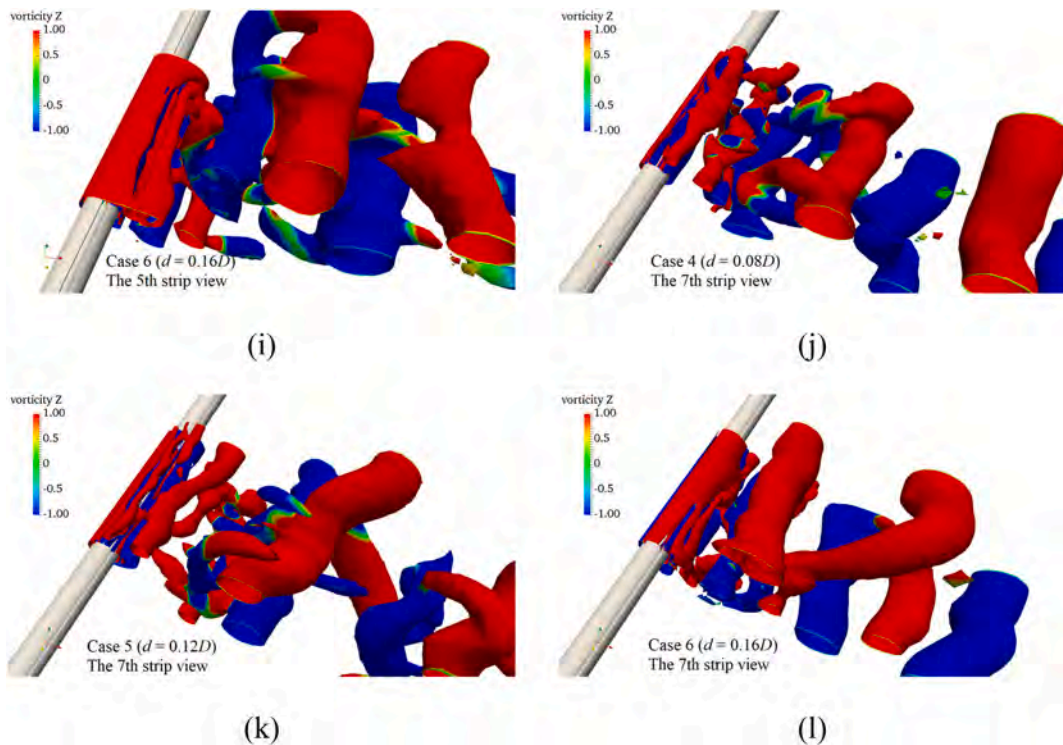
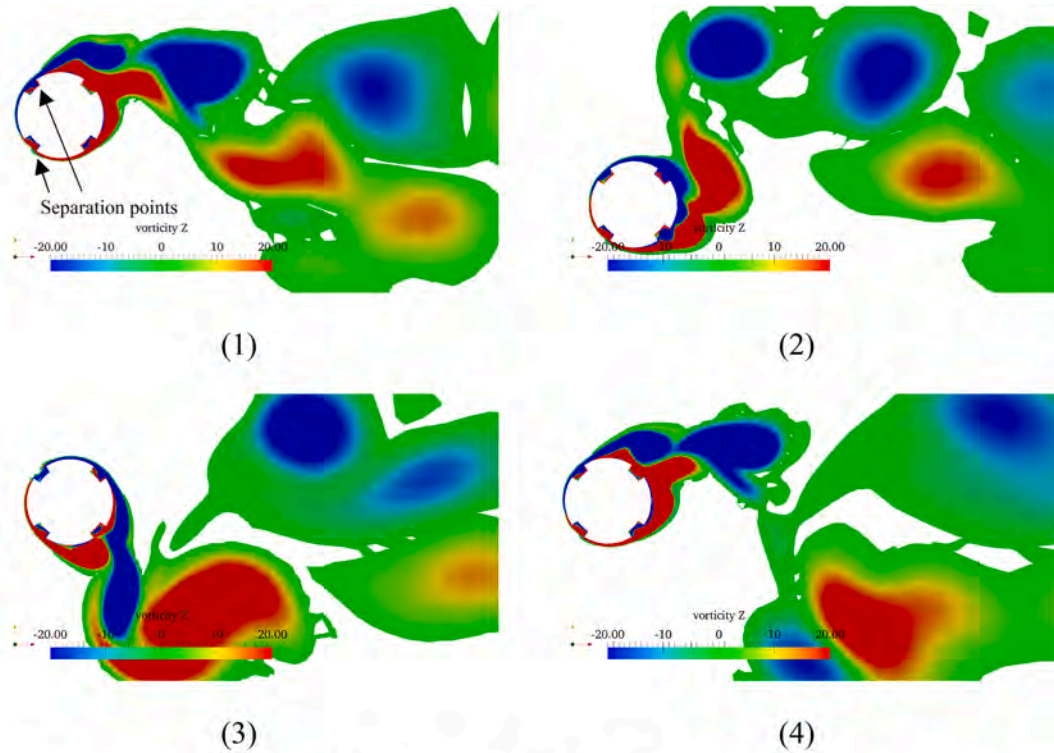


Fig. 15. (continued).

application of grooves, vortex fusion phenomenon can be observed in Figs. 11(a-2) where the left part of the shedding positive vortex merges with the new vortex generated in the downstream groove and similar phenomena can also be observed in Figs. 11(b-4) and Fig. 11(c-3), which leads to the more complicated vortex shedding phenomenon than that of the smooth cylinder. Meanwhile, none obvious “2S” (two single vortex) or “2P” (two pairs of vortices) vortex shedding phenomenon can be observed in all simulations. With the increase of the groove depth, obvious small vortices will be generated in the groove especially at $d = 0.16D$ (Case3) as shown in Fig. 11(c). Small positive and negative vortices generated in the upper and lower grooves respectively, which are opposite to vortices generated outside the grooves, when the cylinder moves across the central position of the simulation domain as shown in Figs. 11(c-4). It will change the distribution of the pressure field around the cylinder and suppress the vibration response of the cylinder.

Comparisons of crossflow and inline RMS displacements among smooth cylinder, experiment of Lehn (2003) [49] and cylinders with different groove depths at configuration B are shown in Fig. 12. It can be found that RMS displacements increase apparently due to the application of spanwise grooves at the configuration B as shown in Fig. 3(b) compared with that of the smooth cylinder. With the increase of the groove depth from $0.08D$ to $0.16D$, the maximum crossflow RMS displacements increase to $0.514D$ (Case4), $0.55D$ (Case5) and $0.587D$ (Case6) respectively. In the inline direction, the maximum RMS displacements at around $z/L = 0.25$ increase to $0.126D$ when $d = 0.08D$, to $0.141D$ when $d = 0.12D$ and to $0.12D$ when $d = 0.16D$. While it increases to $0.127D$, $0.136D$ and $0.146D$ respectively when the groove depth increases from $0.08D$ to $0.16D$. Although the variation tendency presents difference at $0.25L$ in the inline direction, both crossflow and inline vibration responses are enlarged resulting from the modification of the cylinder cross-section at configuration B. Fig. 13 presents comparisons of inline mean vibration displacements among smooth cylinder and cylinder with different groove depths at configuration B. The inline deflection shapes of the cylinder keep the first mode shape at all conditions. The maximum inline displacements increase from $0.652D$ to $0.69D$ with the increase of the groove depth, resulting from the enhancement effects of spanwise grooves at configuration B. It can be concluded that the spanwise grooves will magnify vibration responses of the cylinder in both crossflow and inline directions resulting from its inappropriate configuration.

Comparisons of crossflow modal decomposition results and corresponding modal PSD results among cylinder with different groove depths at configuration B are shown in Fig. 19 of appendix. The inline vibration presents the first dominant vibration mode in all groove depths conditions and the time-history modal weight of the first vibration mode are comparatively larger than that of the smooth cylinder. Modal weights of higher modes are smaller than that of the first mode, which contribute to the single mode vibration phenomenon during the whole vibration process of the flexible cylinder. The main parameters of results are listed in Table 5. The dominant vibration frequency corresponding to the dominant vibration mode are 1.697 Hz, 1.696 Hz and 1.702 Hz respectively with the increase of the groove depth. The decrements of dominant vibration frequencies are -0.772% , -0.713% and -1.069% respectively. It can be concluded that the spanwise grooves at configuration B contribute none suppression effects to crossflow vibration frequency features of the flexible cylinder. On the other hand, the comparison of the amplitude of dominant vibration frequency also indicates that it increases with the groove depth.



(a) Case4 ($d = 0.08D$), $z = 5.3$ m: (1) $t = 46.0$ s; (2) $t = 46.2$ s; (3) $t = 46.4$ s; (4) $t = 46.6$ s

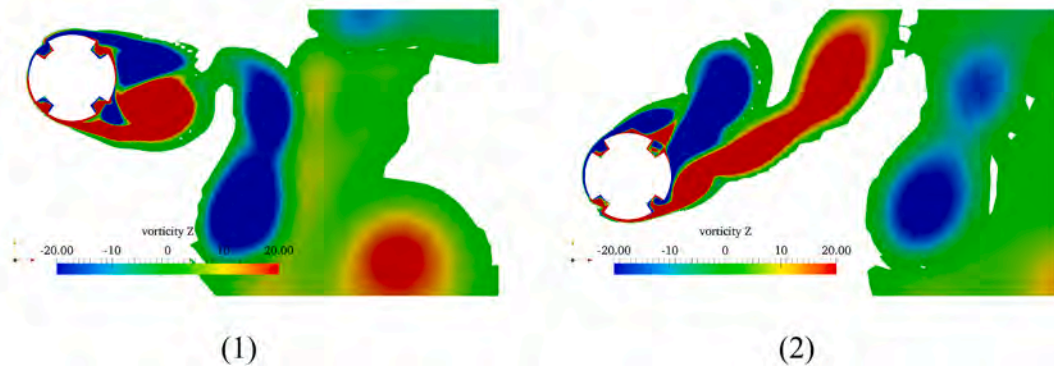
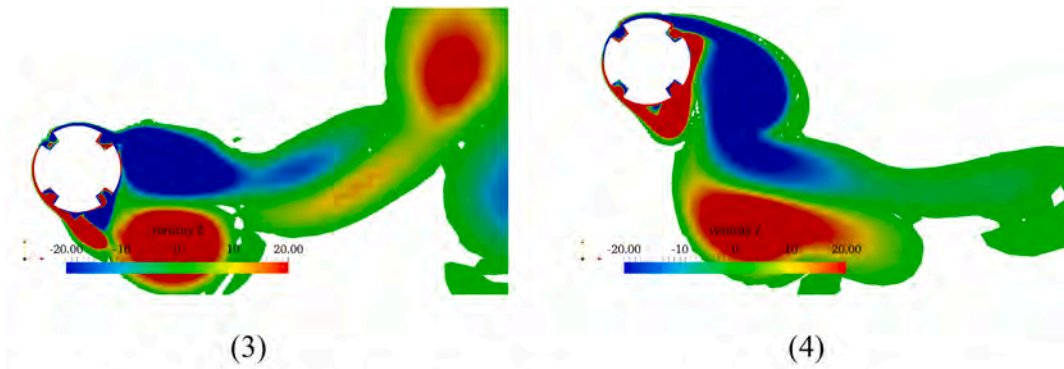


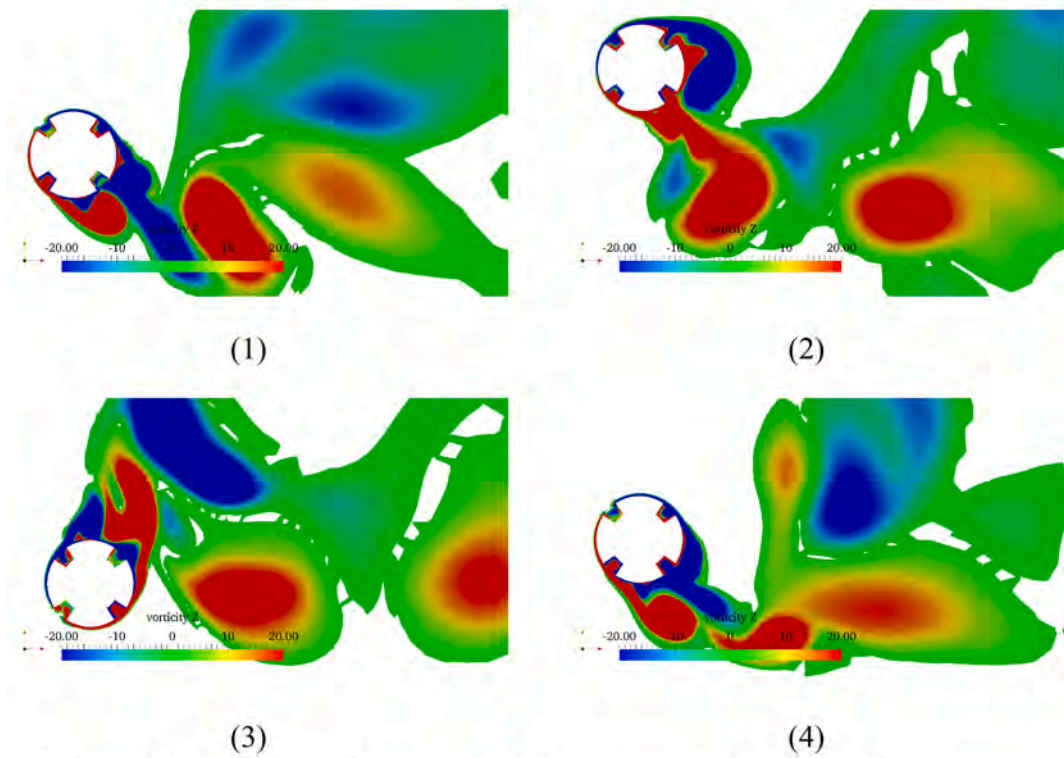
Fig. 16. Instantaneous vorticity- z ($\omega_z = \frac{dv}{dx} - \frac{du}{dy}$) contours at the same axial location along the cylinder with different groove depths at configuration B.

Comparisons of inline vibration decomposition results and corresponding PSD results among cylinders with different groove depths at configuration B are shown in Fig. 20 of appendix. The flexible cylinder presents the single mode vibration phenomenon in the inline direction during the vibration process through comparing time-history modal weights among all vibration modes, which is the same as that in the crossflow direction. The second mode is the dominant vibration mode in the inline direction. The main parameters of results are listed in Table 6. The dominant inline vibration frequencies are 3.452 Hz (Case4), 3.437 Hz (Case5) and 3.402 Hz (Case6) with the groove depth increased from $0.08D$ to $0.16D$, which are close to the inline vibration frequency of the smooth cylinder. While, decrements of the inline vibration frequencies are -1.529% , -1.088% and -0.0588% respectively. Therefore, the spanwise grooves at configuration B present slightly enhancement effects to the inline vibration responses, which is the same as that of the crossflow vibration responses.

Comparisons of vibration trajectories at nine positions along the cylinder span among cylinders with different groove depths at



(b) Case5 ($d = 0.12D$), $z = 5.3$ m: (1) $t = 46.0$ s; (2) $t = 46.2$ s; (3) $t = 46.4$ s; (4) $t = 46.6$ s



(c) Case6 ($d = 0.16D$), $z = 5.3$ m: (1) $t = 46.0$ s; (2) $t = 46.2$ s; (3) $t = 46.4$ s; (4) $t = 46.6$ s

Fig. 16. (continued).

configuration B are shown in Fig. 14. Comparing with vibration trajectories of the smooth cylinder in Fig. 9(a), both the inline and the crossflow vibration regions are widened that leads to the increase of the inline and crossflow vibration RMS values corresponding to the comparison as shown in Fig. 12. All vibration trajectories keep the long strip shape with slight radian to both upward and downward direction especially at $z/L = 0.5$ where inline vibration reaches the stagnation point of the second inline vibration mode. The phase lag phenomenon between the inline and crossflow vibrations at lower and upper parts of the cylinder lead to the generation of the “V” shape and inverse “V” shape of vibration trajectories, while none “8” shape of vibration trajectory is observed compared with the smooth cylinder. The crossflow vibration reaches around zero when the inline vibration reaches its minimum position that leads to the generation of bottom part of the “V” trajectory. The crossflow vibration reaches its minimum or maximum positions when the

inline vibration reaches its maximum position that leads to the generation of the left and right parts of the “V” trajectory. The generation of the inverse “V” shape of vibration trajectory follows similar vibration phenomenon. Meanwhile, obvious “V” shape, inverse “V” shape and mixed shape (both “V” shape and inverse “V” shape appear during the long interval) of vibration trajectories can be observed at lower and upper parts of the cylinder especially when the groove depth increases to $0.16D$ (Case6). It can be concluded that spanwise grooves at configuration B play none suppression effects but enhancement effects on VIV responses of the flexible cylinder, which is similar to the VIV magnification phenomenon as presented in hydro-energy harvesting investigations of Zhao et al. (2020).

Corresponding instantaneous iso-surface of Q-criterion ($Q = 5$) colored by vorticity- z at $t = 47$ s among three groove depths are shown in Fig. 15. It can be found that the width of the wake street is obviously widened especially at the 5th strip compared with Fig. 10. Although cylindrical shape of vortices can still be observed far from the cylinder, more discrete small vortices are generated and shed near the cylinder surface as shown in Fig. 15(h) and (i). The wavy shape of vortices can be observed in all cases where a whole vortex shed from the cylinder without separation along the axial direction. However, with the increase of the groove depth, vortices become discrete before shedding from the cylinder that leads to the generation of small vortices and chaos vortex shedding phenomenon similar to that shown in Fig. 10. Phenomenon of a cylindrical shape of vortex surrounded by several small curved strip vortices can be observed in Fig. 15(d) and (g), which may result from the discrete small vortices generated at the back of the cylinder and stretched under the rotation of vortex shedding.

Instantaneous vorticity- z contours at $z = 5.3$ m along the cylinder span among cylinders with different groove depths at configuration B are shown in Fig. 16. It can be found that the width of the vortex street shown in Fig. 16 is wider than that in Fig. 11 for the same groove depth condition, which means that the vortex shedding phenomenon for spanwise grooves arranged at configuration B becomes more violent leading to the enhancement of the cylinder vibration. The separation points move to the right edge of the top left and lower left grooves as shown in Figs. 16(a-1), which leads to the change of vortex distribution around the cylinder surface. During the vibration of the cylinder, almost three quarters of the cylinder surface are occupied by the positive or negative vortex as shown in Figs. 16(a-4), (b-4) and (c-4). Then the pressure difference alongside the vibration direction will be strengthened and contributes to the enhancement of vibration, especially when the groove depth increases to $0.16D$.

5. Conclusions

Numerical investigations on VIV suppression effects of spanwise grooves attached to the flexible cylinder at two configurations experiencing the uniform flow have been carried out using the viv3D-FOAM-SJTU solver. The groove width keeps a constant as $0.2D$ and the groove depth varies from $0.08D$ to $0.16D$. Detailed comparisons of vibration RMS displacements, modal responses, vibration frequency responses and three-dimensional wake fields have been carried out among smooth cylinder and grooved cylinders. The conclusions are summarized as follows.

- 1) VIV suppression effects of spanwise grooves are sensitive to its configurations. Significant suppression effects can be observed in both crossflow and inline vibration RMS displacements when four spanwise grooves are arranged at configuration A where two grooves are parallel to the incoming uniform flow direction. While vibration responses are strengthened when spanwise grooves are arranged at configuration B;
- 2) The spanwise grooves with groove depth $d = 0.16D$ at configuration A present the best VIV suppression effects. While the same groove geometry at configuration B present the strongest VIV enhancement effects. Moreover, the spanwise grooves at two configurations play little effects on VIV frequency responses in both directions.
- 3) The VIV suppression or enhancement effects of spanwise grooves mainly result from the interference effects of the vortex shedding and pressure difference distribution around the cylinder surface.

Declaration of competing interest

The authors declare the following financial interests/personal relationships which may be considered as potential competing interests: Decheng Wan reports financial support was provided by Shanghai Jiao Tong University.

Data availability

Data will be made available on request.

Acknowledgements

This work was supported by the National Natural Science Foundation of China (52131102), and the National Key Research and Development Program of China (2019YFB1704200), to which the authors are most grateful.

Appendix

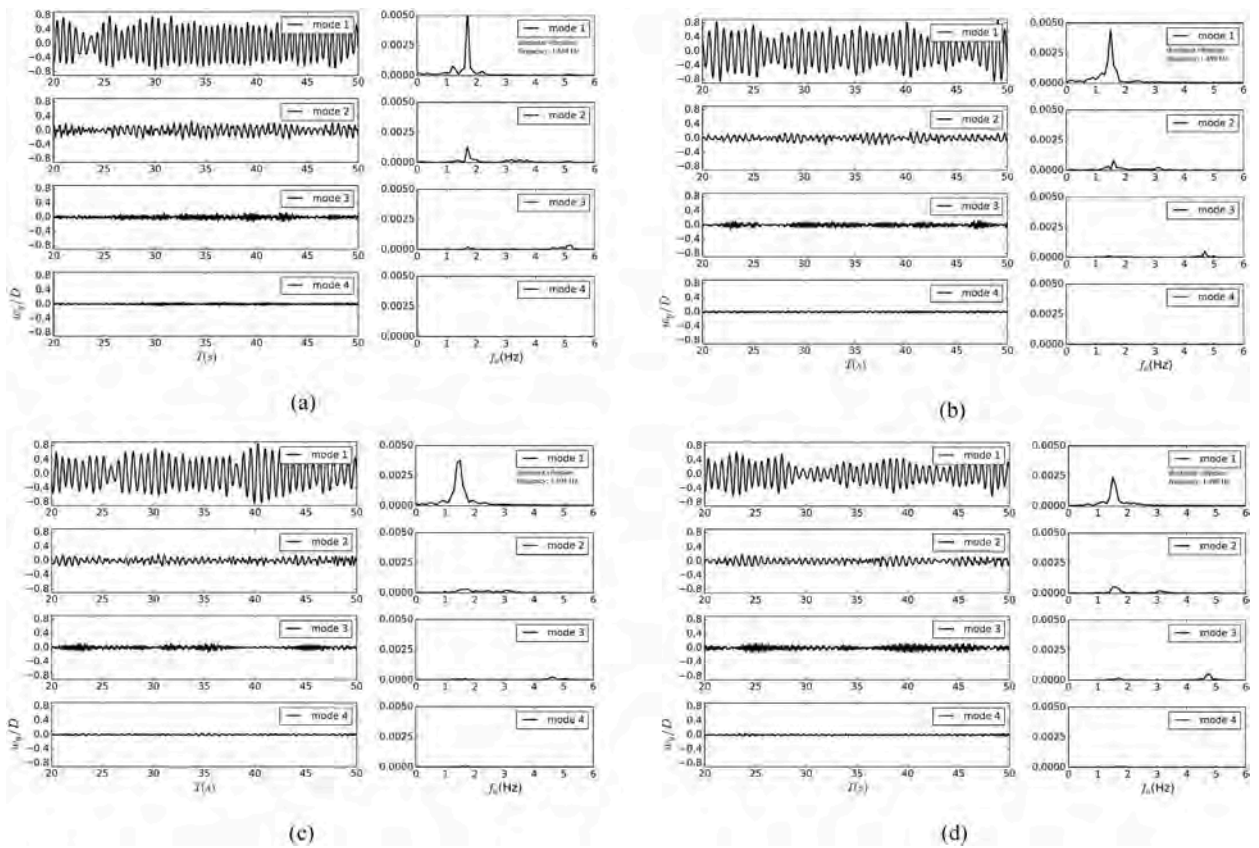


Fig. 17. Comparisons of crossflow modal weights and corresponding PSD among smooth cylinder and cylinders with different groove depths at configuration A: (a) smooth cylinder; (b) Case1 ($d = 0.08D$); (c) Case2 ($d = 0.12D$); (d) Case3 ($d = 0.16D$).

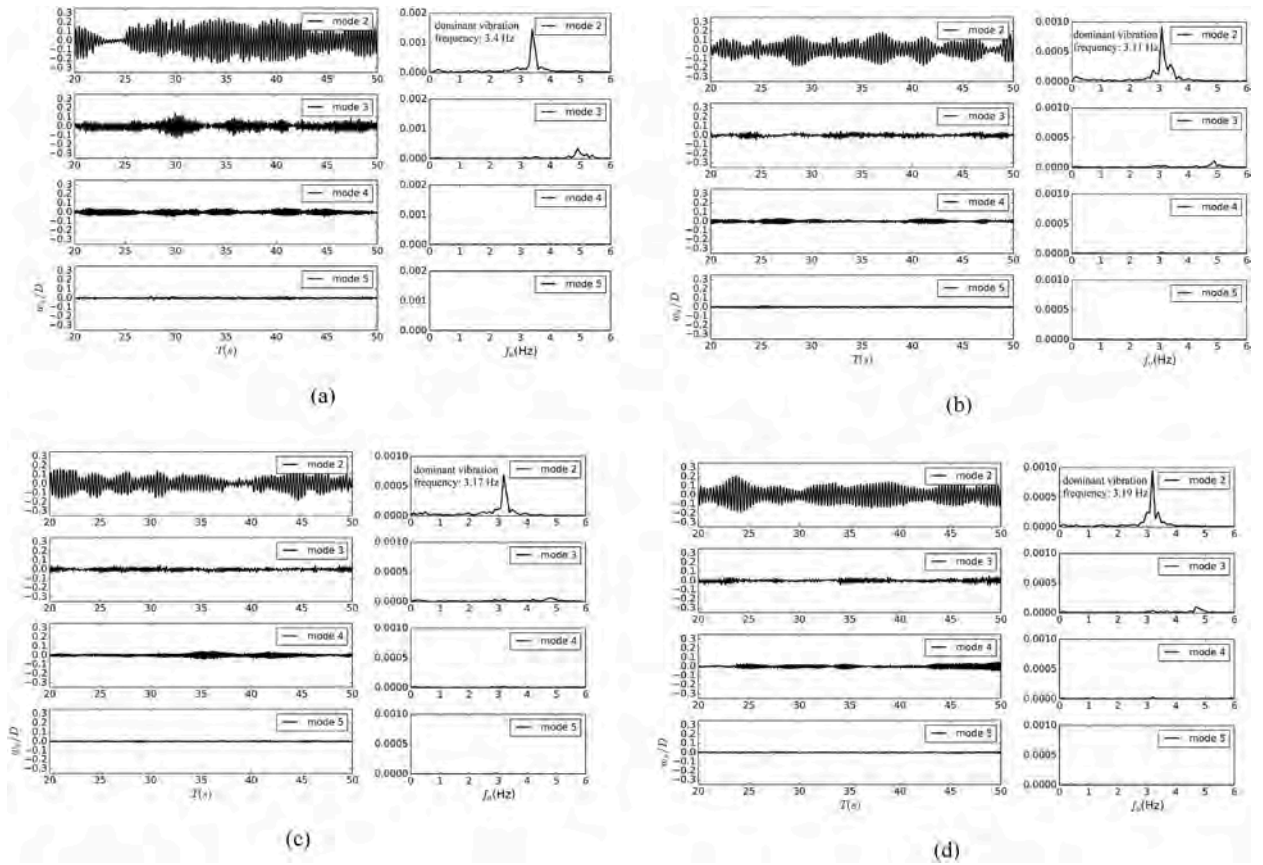


Fig. 18. Comparisons of inline modal weights and corresponding PSD among smooth cylinder and cylinders with different groove depths at configuration A: (a) smooth cylinder; (b) Case1 ($d = 0.08D$); (c) Case2 ($d = 0.12D$); (d) Case3 ($d = 0.16D$).

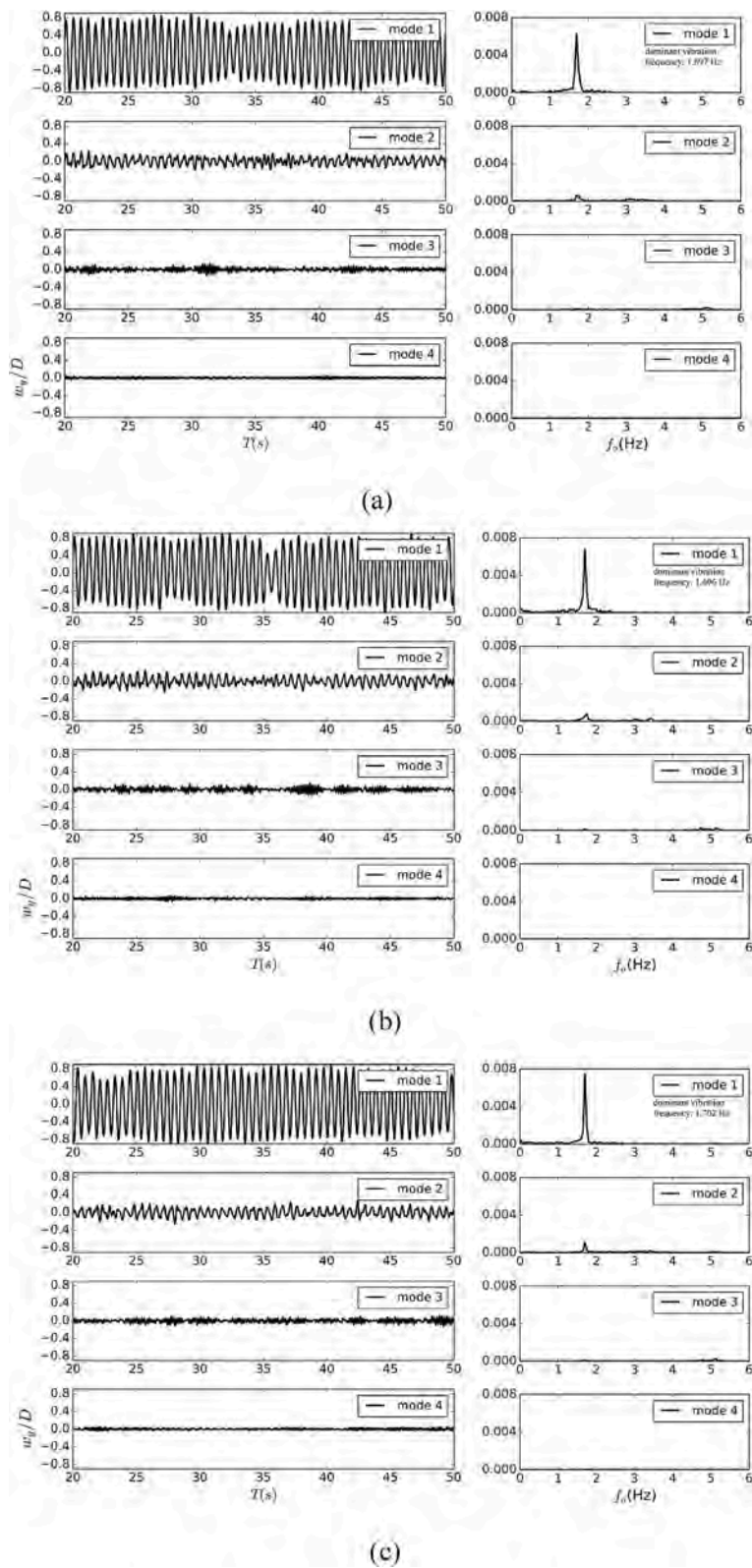
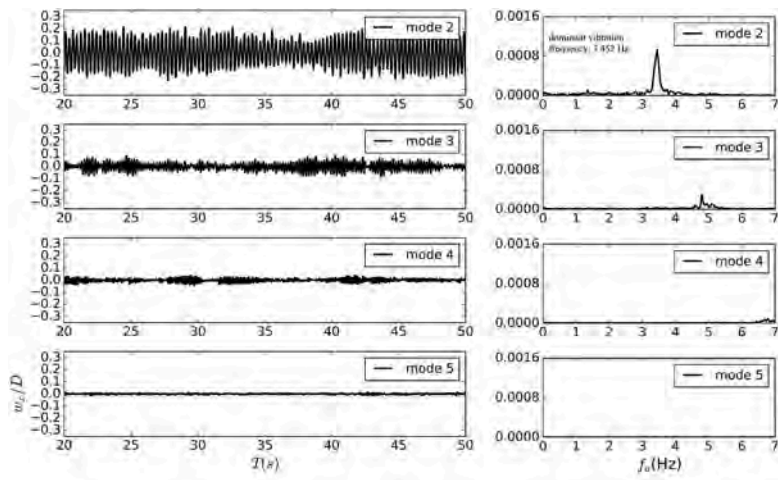
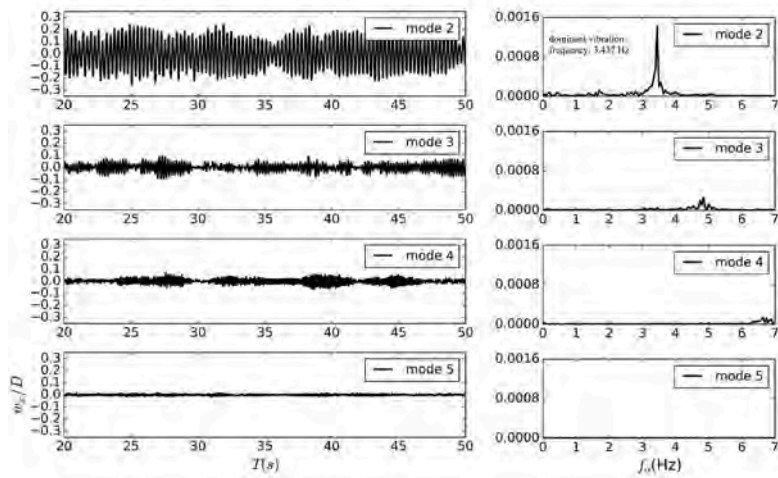


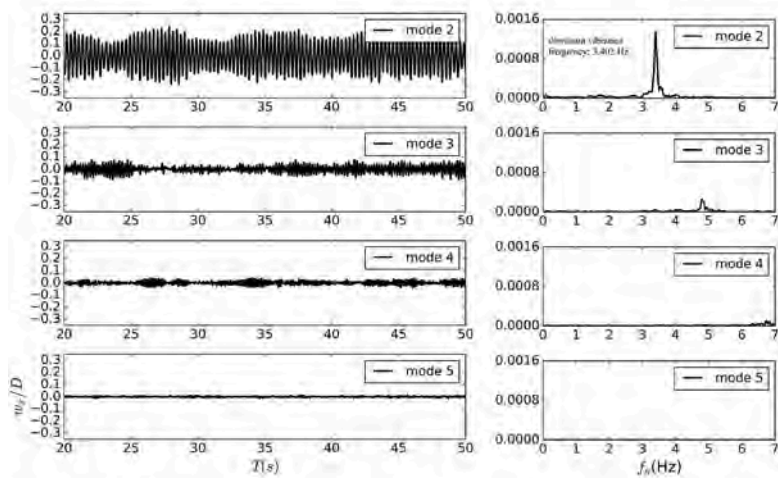
Fig. 19. Comparisons of crossflow modal weights and corresponding PSD among cylinders with different groove depths at configuration B: (a) Case4 ($d = 0.08D$); (b) Case5 ($d = 0.12D$); (c) Case6 ($d = 0.16D$).



(a)



(b)



(c)

(caption on next page)

Fig. 20. Comparisons of inline modal weights and corresponding PSD among cylinders with different spanwise grooves at configuration B: (a) Case4 ($d = 0.08D$); (b) Case5 ($d = 0.12D$); (c) Case6 ($d = 0.16D$).

References

- [1] Bearman PW. Vortex shedding from oscillating bluff bodies. *Annu Rev Fluid Mech* 1984;16:195–222.
- [2] Sumer BM, Fredsøe J. *Hydrodynamics around cylindrical structures*[M]. World Scientific; 1997.
- [3] Sarpkaya T. A critical review of the intrinsic nature of vortex-induced vibrations. *J Fluid Struct* 2004;19:389–447.
- [4] Gabbai RD, Benaroya H. An overview of modeling and experiments of vortex-induced vibration of circular cylinders. *J Sound Vib* 2005;282(3–5):575–616.
- [5] Williamson CHK, Govardhan R. Vortex-induced vibrations. *Annu Rev Fluid Mech* 2004;36:413–55.
- [6] Williamson CHK, Govardhan R. A brief review of recent results in vortex-induced vibration. *J Wind Eng Ind Aerod* 2008;96:713–35.
- [7] Huang XD, Zhang H, Wang XS. An overview on the study of vortex-induced vibration of marine riser. *Journal of Marine Sciences* 2009;27(4):95–101.
- [8] Wu X, Ge F, Hong Y. A review of recent studies on vortex-induced vibrations of long slender cylinders. *J Fluid Struct* 2012;28:292–308.
- [9] Chen WM, Fu YQ, Guo SX, et al. Fluid-solid coupling and hydrodynamic response of vortex-induced vibration of slender ocean cylinders. *Advances in Mechanics* 2016;38(5):604.
- [10] Wan DC, Duanmu YA. Recent review of numerical studies on vortex-induced vibrations of long slender flexible risers in deep sea. *Chin Q Mech* 2017;38(2):179–96.
- [11] Wu CJ, Wang L, Wu JZ. Suppression of the von kármán vortex street behind a circular cylinder by a travelling wave generated by a flexible surface. *J Fluid Mech* 2007;574:365–91.
- [12] Korkischko I, Meneghini JR. Suppression of vortex-induced vibration using moving surface boundary-layer control. *J Fluid Struct* 2012;34(3):259–70.
- [13] Chen WL, Xin DB, Xu F, et al. Suppression of vortex-induced vibration of a circular cylinder using suction-based flow control. *J Fluid Struct* 2013;42(4):25–39.
- [14] Feng LH, Wang JJ, Pan C. Effect of novel synthetic jet on wake vortex shedding modes of a circular cylinder. *J Fluid Struct* 2010;26:900–17.
- [15] Zhou T, Razali SFM, Hao Z, et al. On the study of vortex-induced vibration of a cylinder with helical strakes. *J Fluid Struct* 2011;27(7):903–17.
- [16] Ranjith ER, Sunil AS, Pauly L. Analysis of flow over a circular cylinder fitted with helical strakes. *Procedia Technology* 2016;24:452–60.
- [17] Gao Y, Yang JD, Xiong YM, et al. Experimental investigation of the effects of the coverage of helical strakes on the vortex-induced vibration response of a flexible riser. *Appl Ocean Res* 2016;59:53–64.
- [18] Trim AD, Braaten H, Lie H, et al. Experimental investigation of vortex-induced vibration of long marine risers. *J Fluid Struct* 2005;21(3):335–61.
- [19] Vandiver JK, Swithenbank S, Jaiswal V, et al. The effectiveness of helical strakes in the suppression of high-mode-number VIV[C]. In: *Offshore technology conference*; 2006. May 1–4, Houston, Texas, USA.
- [20] Bourguet R, Modarres-Sadeghi Y, Karniadakis GE, et al. Wake-body Resonance of long flexible structures is dominated by Counterclockwise orbits. *Phys Rev Lett* 2011;107(13):134502.
- [21] Quen LK, Abu A, Kato N, et al. Investigation on the effectiveness of helical strakes in suppressing VIV of flexible riser. *Appl Ocean Res* 2014;44:82–91.
- [22] Quen LK, Abu A, Kato N, et al. Performance of two- and three-start helical strakes in suppressing the vortex-induced vibration of a low mass ratio flexible cylinder. *Ocean Eng* 2018;166:253–61.
- [23] Xu WH, Luan YS, Han QH, et al. The effect of yaw angle on VIV suppression for an inclined flexible cylinder fitted with helical strakes. *Appl Ocean Res* 2017;67:263–76.
- [24] Ren HJ, Xu YW, Cheng JY, et al. Vortex-induced vibration of flexible pipe fitted with helical strakes in oscillatory flow. *Ocean Eng* 2019;189:106274.
- [25] Song ZH, Duanmu L, Gu JJ. Numerical investigation on the suppression of VIV for a circular cylinder by three small control rods. *Appl Ocean Res* 2017;64:169–83.
- [26] Zhu HJ, Yao J, Ma Y, et al. Simultaneous CFD evaluation of VIV suppression using smaller control cylinders. *J Fluid Struct* 2015;57:66–80.
- [27] Lu Y, Liao YY, Liu B, et al. Cross-flow vortex-induced vibration reduction of a long flexible cylinder using 3 and 4 control rods with different configurations. *Appl Ocean Res* 2019;91:101900.
- [28] Li P, Liu LH, Dong ZK, et al. Investigation on the spoiler vibration suppression mechanism of discrete helical strakes of deep-sea riser undergoing vortex-induced vibration. *Int J Mech Sci* 2020:105410.
- [29] Nikoo HM, Bi K, Hao H. Effectiveness of using pipe-in-pipe (PIP) concept to reduce vortex-induced vibrations (VIV): three-dimensional two-way FSI analysis. *Ocean Eng* 2018;148:263–76.
- [30] Hu ZM, Wang JS, Sun YK, et al. Flow-induced vibration suppression for a single cylinder and one-fixed-one-free tandem cylinders with double tail splitter plates. *J Fluid Struct* 2021;106:103373.
- [31] Huang S. VIV suppression of a two-degree-of-freedom circular cylinder and drag reduction of a fixed circular cylinder by the use of helical grooves. *J Fluid Struct* 2011;27(7):1124–33.
- [32] Law YZ, Jaiman RK. Passive control of vortex-induced vibration by spanwise grooves. *J Fluid Struct* 2018;83:1–26.
- [33] Zhou B, Wang XK, Guo W, et al. Experimental measurements of the drag force and the near-wake flow patterns of a longitudinally grooved cylinder. *J Wind Eng Ind Aerod* 2015;145:30–41.
- [34] Canpolat C, Sahin B. Influence of single rectangular groove on the flow past a circular cylinder. *Int J Heat Fluid Flow* 2017;64(Apr):79–88.
- [35] Wang W, Song BW, Mao ZY, et al. Numerical investigation on VIV suppression of marine riser with triangle groove strips attached on its surface. *Int J Nav Archit Ocean Eng* 2019;11:875–82.
- [36] Zhao GF, Xu JK, Duan K, et al. Numerical analysis of hydroenergy harvesting from vortex-induced vibrations of a cylinder with groove structures. *Ocean Eng* 2020;218:108219.
- [37] Deng D, Zhao WW, Wan DC. Vortex-induced vibration prediction of a flexible cylinder by three-dimensional strip model. *J Ocean Engineering* 2020;205:107318.
- [38] Hu H, Zhao WW, Wan DC. Vortex-induced vibration of a slender flexible riser with grooved and spanwise strips subject to uniform currents. *Phys Fluids* 2022;34:125131.
- [39] Hu H, Pan Z, Zhao WW, et al. Numerical investigation of vortex-induced vibrational responses to a flexible tensioned riser with symmetric grooves in uniform currents. *Ocean Eng* 2023;271:113780.
- [40] Duanmu Y, Zou L, Wan DC. Numerical simulations of vortex-induced vibrations of a flexible riser with different aspect ratios in uniform and shear currents. *Journal of Hydrodynamics, Ser. B* 2017;29(6):1010–22.
- [41] Duanmu Y, Zou L, Wan DC. Numerical analysis of multi-modal vibrations of a vertical riser in step currents. *Ocean Eng* 2018;152:428–42.
- [42] Fu BW, Zou L, Wan DC. Numerical study of vortex-induced vibrations of a flexible cylinder in an oscillatory flow. *J Fluid Struct* 2018;77:170–81.
- [43] Menter FR. Zonal two equation $k-\omega$ turbulence models for aerodynamic flows[R]. 1993. AIAA-93-2906.
- [44] Chaplin JR, Bearman PW, Hueru Huarte FJ, et al. Laboratory measurements of vortex-induced vibrations of a vertical tension riser in a stepped current. *J Fluid Struct* 2005;21(1):3–24. SPEC. ISS.

- [45] Zhao WW, Wan DC. Numerical study of 3D flow past a circular cylinder at subcritical Reynolds number using SST-DES and SST-URANS. *Chinese Journal of Hydrodynamics* 2016;31(1):1–8.
- [46] Willden RHJ, Graham JMR. Multi-modal vortex-induced vibrations of a vertical riser pipe subject to a uniform current profile. *Eur J Mech B* 2004;23(1):209–18.
- [47] Bao Y, Palacios R, Graham M, et al. Generalized thick strip modelling for vortex-induced vibration of long flexible cylinders. *J Comput Phys* 2016;321(800):1079–97.
- [48] Bao Y, Zhu HB, Huan P, et al. Numerical prediction of vortex-induced vibration of flexible riser with thick strip method. *J Fluid Struct* 2019;89:166–73.
- [49] Lehn E. VIV suppression tests on high L/D flexible cylinders. Trondheim, Norway: Norwegian Marine Technology Research Institute; 2003.
- [50] Wang E, Xiao Q. Numerical simulation of vortex-induced vibration of a vertical riser in uniform and linearly sheared currents. *Ocean Eng* 2016;121:492–515.